KINETICS OF INTERNAL OXIDATION OF FE-MN-CR STEEL ALLOYS

MASTER THESIS

By

Yao Ma

Thesis committee:	Dr. ir. Wim G. Sloof	TU Delft
	Dr. Yaiza Gonzalez-Garcia	TU Delft
	Ir. William Mao	TU Delft

AUGUST 4, 2017

MATERIALS SCIENCE AND ENGINEERING
Faculty of Mechanical, Maritime and Materials Engineering, Delft University of Technology

ABSTRACT

Selective oxidation behaviour of Fe-Mn-Cr steel alloys annealed at 950°C in Ar plus 5 vol.% H_2 atmosphere under different annealing time and dew points was studied. The Fe-Mn-Cr steel alloys are externally oxidized when annealing at dew point of -45 °C, while internally oxidized at dew points of -10 and 10 °C. The internal oxides formed in the Fe-Mn-Cr steel alloys are (Mn, Fe)O and $(Cr, Mn, Fe)_3O_4$. The kinetics of internal oxidation of Fe-Mn-Cr alloys at 950 °C is diffusion controlled and follows parabolic growth rate law. The measured kinetics of internal oxidation of Fe-Mn-Cr alloys and the concentration depth profiles of internal oxides are in good agreement with simulation results. Adding Cr to the Fe-Mn steel alloys decreases the kinetics of internal oxidation. The growth rate of internal oxidation zone can be predicted by a modified Wagner's internal oxidation model. The external oxides formed during annealing of Fe-Mn-Cr steel alloys cannot be reduced by H_2. However, an oxide-free steel surface can be obtained by first forming and then reducing a Wüstite scale.

Keywords: Internal oxidation, Fe-Mn-Cr steel alloys, kinetics, annealing

TABLE OF CONTENTS

CHAPTER 1

INTRODUCTION

1.1 Project Background

In recent years, the necessity of reducing human induced greenhouse gasses is the direct driving force in the modern automobile industry to develop lighter and stiffer vehicles. Reducing the weight of vehicle's body as well as other outer panels have been proved to be an effective way of reducing fuel consumption and carbon dioxide emission[1-5]. To meet demands regarding crash safety, light weight and other performance appealing to customers, Advanced High Strength Steels (AHSS) is rapidly developed.

AHSS is characterized by improved formability and crash safety compared to conventional steels, with yield strength higher than 300 MPa and tensile strength higher than 600 MPa [5]. The high strength depends on multiple aspects such as selected chemical compositions, required microstructures and specific heating and cooling process parameters. Alloying elements like Si, Mn, Al and Cr are added into the AHSS to achieve certain microstructure and properties. It is known that the transformation of retained austenite increases the work hardening rate of steel and obtained higher ductility[6, 7]. Manganese is an important austenite stabilizer[8] and helped to obtain a good combination of strength and formability.

However, poor corrosion resistance is the major limitation of AHSS application in modern automobile industry. To solve this problem, hot dip galvanizing (HDG)[9-11] is applied to the AHSS production lines as one of the most extensively used methods to protect steel sheets from corrosion. In continuous hot dip galvanizing line (CGL)[12], prior to hot dip, a short-term annealing is necessary to deal with recrystallization effect after cold rolling and reduce the iron oxides[9]. In actual

industrial working conditions (see Figure 1.1), the zinc bath temperature is approximately 460 ºC[11] and in continues annealing process, annealing temperature should be higher than the zinc bath. The annealing gas atmosphere is 5 to 10 vol.% hydrogen balanced in nitrogen[4]. According to Figure 1.2, since alloying elements, Mn, Cr, Si, Al have a greater affinity for oxygen than iron, the water vapor will contribute to the oxidation of the minor alloy elements inside the AHSS. Due to the selective oxidation phenomenon, alloying elements are enriched and formed stable oxides on the steel surface. Thus, the selective oxidation phenomenon leads to poor wettability and adhesion between the liquid zinc and the steel surface, which causes degradation of zinc layer[13] and zinc coating defects such as bare spots[9].

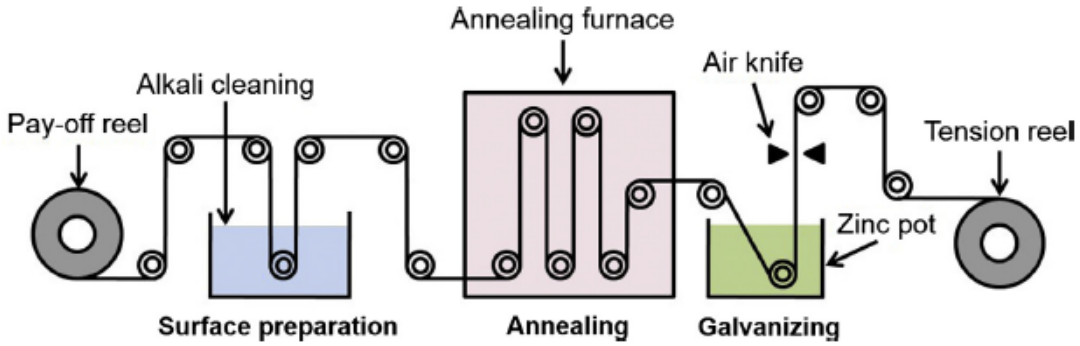

Figure 1.1 schematic view of the hot-dip galvanizing process[12].

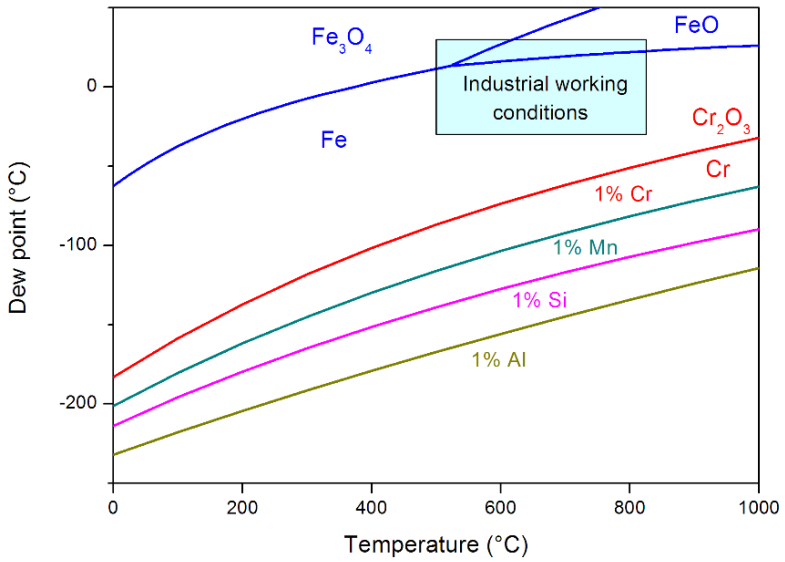

Figure 1.2 Stability diagram for iron and alloying elements annealed in an N_2 + 5 vol.% H_2 atmosphere, in this diagram mole fraction was considered as an activity (ideal solution)[14]

Many research works have been carried out to solve the selective oxidation problem, such as Swaminathan's [15, 16] and Blumenau's [17] work. The main solution is to transform external oxidation to internal oxidation. Based on Wagner's theory[18], the transition from external to internal oxidation is controlled by oxygen partial pressure (dew point). With higher dew point, the permeability of oxygen into the alloy also increases, promoting internal oxidation. In Lashgari's work [14], the oxygen partial pressure is adjusted in the initial stage of annealing high enough to oxidize iron which forms external oxides that cover the whole surface with the minor alloying elements oxides precipitating underneath, as shown in Figure 1.3 (a). Then in the subsequent annealing process, the reducing atmosphere is reducing for iron but not for alloying elements. Finally, after the annealing process before entering the zinc bath, the steel surface is covered with a pure iron layer free of external oxides, as shown in Figure 1.3 (b).

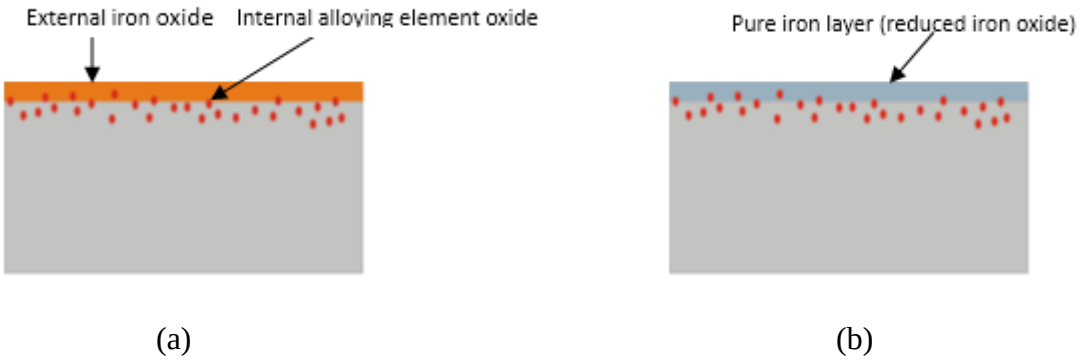

Figure 1.3 Schematic representation of changes of the surface region in an industrial annealing process. (a) formation of FeO at steel surface, (b) reduction of iron oxides.[14]

Knowledge of the oxidation behavior of AHSS under industrial galvanizing line conditions is essential to implement this solution. An analysis on internal and external oxidation of Mn in Fe-Mn binary alloys below the dissociation oxygen partial pressure of FeO was reported in an earlier study[14]. MnO is the main precipitate and the kinetics of internal oxidation in Fe-Mn alloy are diffusion controlled and obey parabolic growth rate law (see Figure 1.4). The oxidation behavior of Mn in Fe-Mn binary alloys can be predicted by classical internal oxidation theory. However, classical internal oxidation theory is based on binary alloy, the knowledge about the

prediction of oxidation behavior in ternary alloy system is limited. Adding the third element changes the alloying elements activity and oxygen solubility. Furthermore, it increases the complexity in analyzing the diffusion mechanisms. The oxidation rate of alloys is determined both by thermodynamic and kinetic considerations. A thermodynamic study focusing on investigating the composition of the oxides formed in Fe-Mn-Cr ternary steel alloy as a function of alloy composition and the oxygen partial pressure was reported[23]. The addition of element Cr leads to the formation of $MnCr_2O_4$ spinel oxide and promotes the formation of external oxides.

In this thesis, the main aim is to analyze the kinetics of oxidation of Fe-Mn-Cr alloy. Furthermore, the effect of dew point, as well as alloy composition on the selective oxidation phenomena, is studied. The experimental results are compared with simulation results based on an oxidation model.

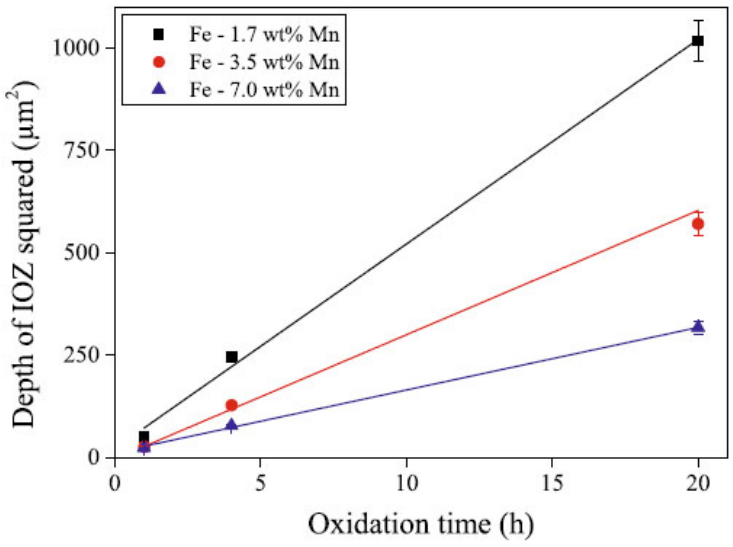

Figure1.4 Internal oxidation kinetics of Mn in steel alloys oxidized at 950 ºC in a gas mixture of N_2 + 5 vol % H_2 with a dew point of 10 ºC[14]

1.2 Outline of the thesis

As the beginning, an introduction on advanced high strength steel and galvanize line is addressed. Selective oxidation occurred in continuous hot dip galvanizing process is discussed. In Chapter 2, classical internal oxidation theory and an extension focus on the kinetics of internal oxidation of ternary alloy are studied. Furthermore, a literature review on oxidation of Fe-Mn-Cr alloys below dissociation pO_2 of FeO is given. Experimental approaches such as SEM, EPMA, XRD applied in this study are described in Chapter 3. Then, in Chapter 4, the results on the kinetics of internal oxidation of Fe-Mn-Cr alloys are discussed and compared to the simulaiton results. Finally, in Chapter 5 and 6, the conclusions and some recommendations are given, respectively.

CHAPTER 2

THEORETICAL BACKGROUND

2.1 Wagner's classical theory for internal oxidation

Wagner's oxidation theory[18] has contributed to numerous works on high temperature oxidation research in past decades. The key features of internal oxidation of A-B binary alloy according to Wagner's model are described here.

Consider a binary A-B alloy system, where A is the noble matrix component and B is the more reactive component. If oxygen and the less noble component B have a suitable solubility in matrix A and their diffusivities in the matrix $D_{\mathrm{O}} >> D_{\mathrm{B}}$, then B element can form stable oxides inside the A matrix according to:

$$\mathrm{B} + v\,\mathrm{O} = \mathrm{BO}_v \tag{2.1}$$

Dissolution of oxygen in the alloy can be described by Sievert's law according to Eq. (2.2):

$$N_{\mathrm{O}}{}^{S} = K_S (p_{\mathrm{O}_2})^{1/2} \tag{2.2}$$

, where $N_{\mathrm{O}}{}^{S}$ is the mole fraction of dissolved oxygen in the alloys and at the surface, p_{O_2} is oxygen partial pressure (in atm) in gas ambient. K_S is the Sievert's constant.

In Wagner's model, it is assumed that the internal oxidation is a bulk diffusion-controlled process. [18] Under this assumption, no preferential grain boundary diffusion occurs, the penetration depth ξ of the precipitated oxides as a function of oxidation time *t* can be described by a parabolic growth law.

$$\xi = k_p \sqrt{t} \tag{2.3}$$

, where k_p is the parabolic growth rate constant of internal oxidation. The parabolic growth rate constant is determined by a dimensionless kinetic parameter γ and diffusion coefficient of oxygen in the matrix D_O as:

$$k_p = 2\gamma\sqrt{D_O} \tag{2.4}$$

The distribution of oxygen and solute elements B within the internal oxidation zone could be described by Fick's second law as:

$$\frac{\partial N_i}{\partial t} = D_i \frac{\partial^2 N_i}{\partial x^2}, i = [\mathrm{O}] or [\mathrm{B}] \tag{2.5}$$

, where N_i is the mole fraction of diffusing elements *i* and D_i is the diffusion coefficient of diffusing elements *i* in the base metal.

The dimensionless kinetic parameter γ can be resolved from solving Equation (2.5) when considering appropriate boundary conditions for an extremely low solubility product oxide and the mass balance at the reaction front. In Wagner's model, it is assumed and often the case, for very stable oxide precipitation, the reaction occurs completely and solely at $x=\xi$. The necessary conditions for solving Equation (2.5) are listed below [18]:

For the initial condition, $N_{\mathrm{B}} = N_{\mathrm{B}}{}^{0}$ $(x > 0, t = 0)$ (2.6)

For boundary conditions, $N_{\mathrm{O}} = N_{\mathrm{O}}{}^{\mathrm{S}}$ $(x = 0, t > 0)$ (2.7)

, where $N_{\mathrm{B}}{}^{0}$ is the molar fraction of the element B in the bulk alloy.

For the assumed very stable oxides, the solubility product ($K_{sp} = N_{\mathrm{B}}\, N_{\mathrm{O}}{}^{v}$) is extremely small which means the concentration of dissolved alloying element B within the internal oxidation zone (IOZ) and the concentration of dissolved oxygen beyond IOZ is zero. Thus, it is obtained the following conditions [18]:

For extremely low solubility product, $N_{\mathrm{B}} = 0$ $(x \le \xi, t > 0)$ (2.8)

For extremely low solubility product, $N_{\mathrm{O}} = 0$ $(x \ge \xi, t > 0)$ (2.9)

A schematic illustration of the concentration profiles under above conditions is given in Figure 2.1. Considering the mass balance at the internal oxidation front, a general solution for γ is obtained as[14]:

$$\frac{N_{\mathrm{O}}^{S}}{\nu N_{\mathrm{B}}^{0}} = \frac{\exp(\gamma^2) erf(\gamma)}{\varphi_{\mathrm{B}}^{1/2} \exp(\gamma^2 \varphi_{\mathrm{B}}) erfc(\gamma \varphi_{\mathrm{B}}^{1/2})} \tag{2.10}$$

, where $\varphi_B = \frac{D_O}{D_B}$ and the dependence of the diffusivities D_O and D_B on alloy composition is neglected.

The enrichment of oxide precipitates in IOZ is described by the enrichment factor a_{B}, where $N_{\mathrm{BO_v}}$ is the molar fraction of B oxides in the IOZ. A general solution for a_{B} is obtained as[14]:

$$a_B = \frac{1}{\sqrt{\pi}\gamma \varphi_B^{1/2} \exp(\gamma^2 \varphi_B) erfc(\gamma \varphi_B^{1/2})} \tag{2.11}$$

The calculation of γ can be simplified under two limiting cases:

a) when the permeability of oxygen ($D_{\mathrm{O}} N_{\mathrm{O}}$) is much larger than the permeability of alloying element B ($D_{\mathrm{B}} N_{\mathrm{B}}$), it is obtained $\gamma \varphi_{\mathrm{B}}^{1/2} >> 1$ and $\gamma << 1$. This relationship means that diffusion of oxygen in the alloy is dominant for the kinetics of internal oxidation. Solute enrichment can be neglected since the outward diffusion of solute element B can be neglected. In this case, γ and k_p can be expressed as following Equations:

$$\gamma = \sqrt{\frac{N_{\mathrm{O}}^{S}}{2\nu N_{\mathrm{B}}^{0}}} \tag{2.12}$$

$$k_p = \sqrt{\frac{2N_O{}^S D_O}{\nu N_B{}^0}} \tag{2.13}$$

b) when the permeability of oxygen ($D_O N_O$) is much smaller than the permeability of alloying element B ($D_B N_B$), it is obtained $\gamma \varphi_B{}^{1/2} << 1$ and $\gamma << 1$. This relationship means that both diffusion of oxygen and alloying element in the alloy are dominant for the kinetics of internal oxidation. In this case, γ and k_p can be expressed as following Equations:

$$\gamma = \frac{\pi D_O N_O{}^S}{2\nu D_B N_B{}^0} \tag{2.14}$$

$$k_p = \frac{\pi D_O N_O{}^S}{\nu D_B N_B{}^0} \sqrt{D_O} \tag{2.15}$$

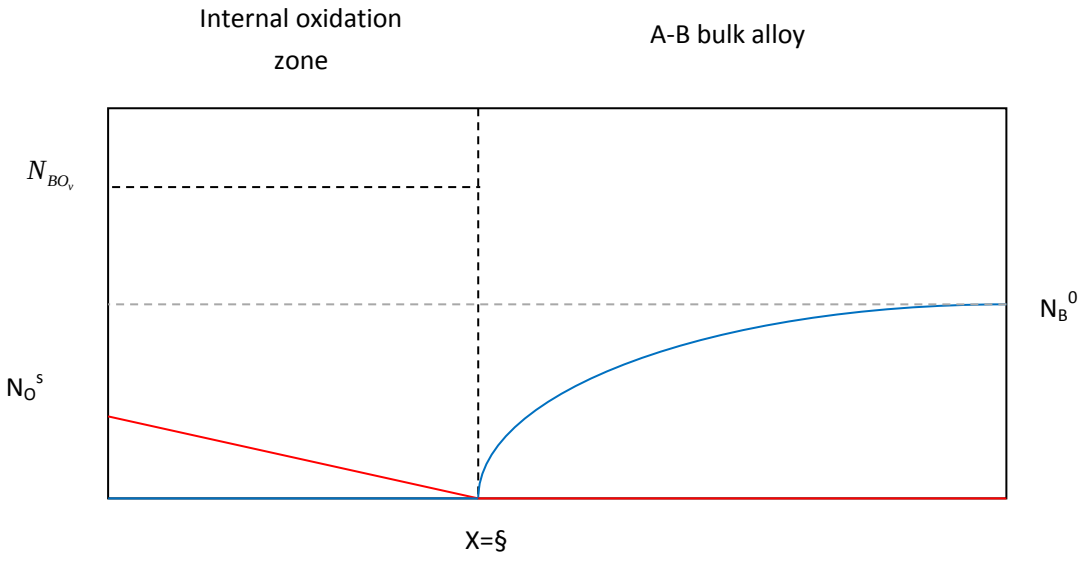

Figure 2.1 Concentration profiles of internal oxidation of A-B binary alloy

2.2 Modified Wagner's internal oxidation theory for ternary alloy

As described above, Wagner's theory could be applied to predict the kinetics of internal oxidation of binary alloys based on several assumptions. In this section, a treatment of the kinetics of internal oxidation of an A-B-C ternary alloy in the absence of an external scale is discussed.

Consider a ternary alloy A-B-C system, where A is the noblest matrix element and C is the most reactive element. Assume the oxygen partial pressure is below the stability of A oxides but above the stability of both B and C oxides. The simplest condition in dealing with internal oxidation of two alloying elements oxidized in the ternary system is that they react with oxygen at same internal oxidation front. As described in section 2.1, the internal oxidation rate is assumed as a diffusion-controlled factor. Thus, solute elements B and C forming BO_v and CO_u precipitated at the single front ($x=\xi$) can be described by a parabolic growth law as shown in Eq. (2.3).

The analysis is assumed that the oxides of both metal solute elements B and C are very stable[20, 21]. In this case, the concentration of two dissolved alloying elements B and C within the internal oxidation zone (IOZ) is zero. Also, the concentration of dissolved oxygen beyond IOZ is zero. A schematic illustration of the concentration profiles under these conditions is given in Figure 2.2.

Due to the complexities of diffusion mechanisms in ternary alloy system, here it is assumed that the diffusivity of each alloying element is considered as constant, independent of alloy composition. This assumption neglects the so-called mixed terms in the diffusion fluxes of the various components in the alloy[21].

The distribution of oxygen and solute elements B and C within the internal oxidation zone could be described by Fick's second law as:

$$\frac{\partial N_i}{\partial t} = D_i \frac{\partial^2 N_i}{\partial x^2}, i = [\mathrm{O}] or [\mathrm{B}] or [\mathrm{C}] \tag{2.16}$$

, where x is the distance to the surface, N_i is the mole fraction of diffusing elements i and D_i is the diffusion coefficient of diffusing elements i in the base metal.

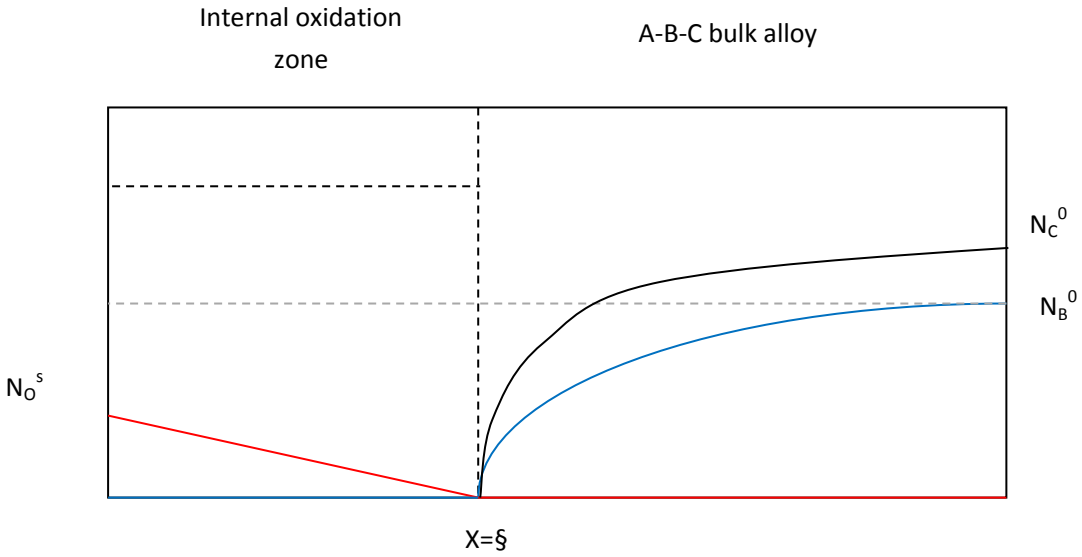

Figure 2.2 Concentration profiles of internal oxidation of A-B-C ternary alloy

Under the boundary conditions illustrated in Figure.2.2, the solutions of Eq. (2.16) are[20, 21]:

$$N_O = N_O^S \left\{ 1 - \frac{erf\left(x / 2\sqrt{D_O t}\right)}{erf\left(\gamma\right)} \right\} \qquad (0 \le x \le \xi) \tag{2.17}$$

$$N_B = N_B^0 \left\{ 1 - \frac{erfc\left(x / 2\sqrt{D_B t}\right)}{erfc\left(\gamma \varphi_B^{1/2}\right)} \right\} \qquad (x \ge \xi) \tag{2.18}$$

$$N_C = N_C^0 \left\{ 1 - \frac{erfc\left(x / 2\sqrt{D_C t}\right)}{erfc\left(\gamma \varphi_C^{1/2}\right)} \right\} \qquad (x \ge \xi) \tag{2.19}$$

, where $\varphi_C = \frac{D_O}{D_C}$, N_O is the mole fraction of dissolved oxygen in the base metal and N_B, N_C are the mole fraction of solute elements B and C, N_B^0, N_C^0 are the mole fraction of solute elements B and C in the bulk alloy.

Mass balance is established at the internal oxidation front between oxygen and alloying elements, namely:

$$J_{O(x=\xi-\varepsilon)} = vJ_{B(x=\xi+\varepsilon)} + uJ_{C(x=\xi+\varepsilon)} \tag{2.20}$$

$$\lim_{\varepsilon\to 0}\left[-D_O\left(\frac{\partial N_O}{\partial x}\right)_{x=\xi-\varepsilon}\right] = vD_B\left(\frac{\partial N_B}{\partial x}\right)_{x=\xi+\varepsilon} + uD_C\left(\frac{\partial N_C}{\partial x}\right)_{x=\xi+\varepsilon} \tag{2.21}$$

Substituting Eqs. (2.17), (2.18) (2.19) into Eq. (2.20), yields[21]

$$N_O^S = vN_B^0\frac{G(\gamma)}{F\left(\gamma\sqrt{\varphi_B}\right)} + uN_C^0\frac{G(\gamma)}{F\left(\gamma\sqrt{\varphi_C}\right)} \tag{2.22}$$

, where $G(w) = \sqrt{\pi}w\exp\left(w^2\right)erf(w), F(w) = \sqrt{\pi}w\exp\left(w^2\right)erfc(w)$

The enrichment of two oxide precipitates in IOZ can be calculated from the expressions given above. The overall degree of enrichment is given by:

$$a_{\text{overall}} = \left[N_B{}^0 a_B + N_C{}^0 a_C\right](N_B{}^0 + N_C{}^0) \tag{2.23}$$

The calculation of γ can be simplified under two limiting cases:

a) when the permeability of oxygen ($D_O N_O$) is much larger than the permeability of alloying element B ($D_B N_B$) and C ($D_C N_C$), it is obtained $\gamma << 1$ and $\gamma\varphi_B{}^{1/2} >> 1, \gamma\varphi_C{}^{1/2} >> 1,$. This relationship means that diffusion of oxygen in the alloy is dominant for the kinetics of internal oxidation. Solute enrichment can

be negligible since the outward diffusion of solute element B can be neglected. For this case, the following asymptotical expansions may be made[20]:

$$\exp(-\gamma^2) \approx 1-\gamma^2 \approx 1$$

$$erf(\gamma) \approx 2\gamma/\sqrt{\pi} \tag{2.24}$$

$$erfc(\gamma\sqrt{\varphi}) \approx \exp(-\gamma^2\varphi)/\sqrt{\pi\varphi}\gamma$$

With the asymptotical expansions above, Eq. (2.22) reduces to:

$$\gamma = \sqrt{\frac{N_{\mathrm{O}}^{\mathrm{S}}}{2(vN_{\mathrm{B}}^{0}+uN_{\mathrm{C}}^{0})}} \tag{2.25}$$

The parabolic rate constant can be written as:

$$k_p = 2\gamma\sqrt{D_{\mathrm{O}}} = \sqrt{\frac{2N_{\mathrm{O}}^{\mathrm{S}}D_{\mathrm{O}}}{vN_{\mathrm{B}}^{0}+uN_{\mathrm{C}}^{0}}} \tag{2.26}$$

b) when the permeability of oxygen ($D_{\mathrm{O}}N_{\mathrm{O}}$) is much smaller than the permeability of alloying element B ($D_{\mathrm{B}}N_{\mathrm{B}}$) and C ($D_{\mathrm{C}}N_{\mathrm{C}}$), it is obtained $\gamma << 1$ and $\gamma\varphi_{\mathrm{B}}^{1/2} << 1, \gamma\varphi_{\mathrm{C}}^{1/2} << 1$. This relationship means that both diffusion of oxygen and alloying element in the alloy are dominant for the kinetics of internal oxidation. For this case, the following asymptotical expansions may be made[20]:

$$\begin{gathered}\exp(-\gamma^2) \approx 1-\gamma^2 \approx 1 \\ erf(\gamma) \approx 2\gamma/\sqrt{\pi} \\ \exp(-\gamma^2\varphi) \approx 1-\gamma^2\varphi \approx 1 \\ erfc(\gamma\sqrt{\varphi}) \approx 1-2\gamma\sqrt{\varphi}/\sqrt{\pi} \approx 1\end{gathered} \tag{2.27}$$

With the asymptotical expansions above, Eq. (2.22) reduces to:

$$\gamma = \sqrt{\frac{N_O^S}{2(\frac{vN_B^0}{\sqrt{\varphi_B \pi}} + \frac{uN_C^0}{\sqrt{\varphi_C \pi}})}} \tag{2.28}$$

The parabolic rate constant can be written as:

$$k_p = 2\gamma\sqrt{D_O} = \sqrt{\frac{2N_O^S D_O}{\frac{vN_B^0}{\sqrt{\varphi_B \pi}} + \frac{uN_C^0}{\sqrt{\varphi_C \pi}}}} \tag{2.29}$$

2.3 Transition from internal oxidation to external oxidation

According to the Wagner's theory, the critical molar fraction of element B in the bulk alloy for transition from internal to external oxidation is [22],

$$N_{\text{critical}} = \left[\frac{\pi g^*}{2\nu} N_O^s \frac{D_O}{D_B} \frac{V_m}{V_{BO_\nu}}\right]^{1/2} \tag{2.30}$$

where g*(~0.3) refers to the critical volume fraction of internal oxide precipitates at which transition from internal to external oxidation takes place. V_m and V_{BO_ν} are the molar volume of alloy and BO_ν oxide, respectively. N_O^s presents the oxygen concentration at alloy surface. If the mole fraction of solute element B is lower than that critical value for the transition from internal to external oxidation, internal oxidation occurs.

2.4 Thermodynamics of oxidation of Fe-Mn-Cr alloys below dissociation oxygen partial pressure of FeO

The phase diagram of Fe-Mn-Cr alloys in an oxidizing environment at 950 °C is shown in Figure. 2.3[23] computed with the thermodynamic tool "FactSage". The phases presented here are as a function of oxygen partial pressure and chromium

content. In this phase, diagram manganese is fixed at 1.8 mol. % and chromium are in a range of 0-1.2 mol. %.

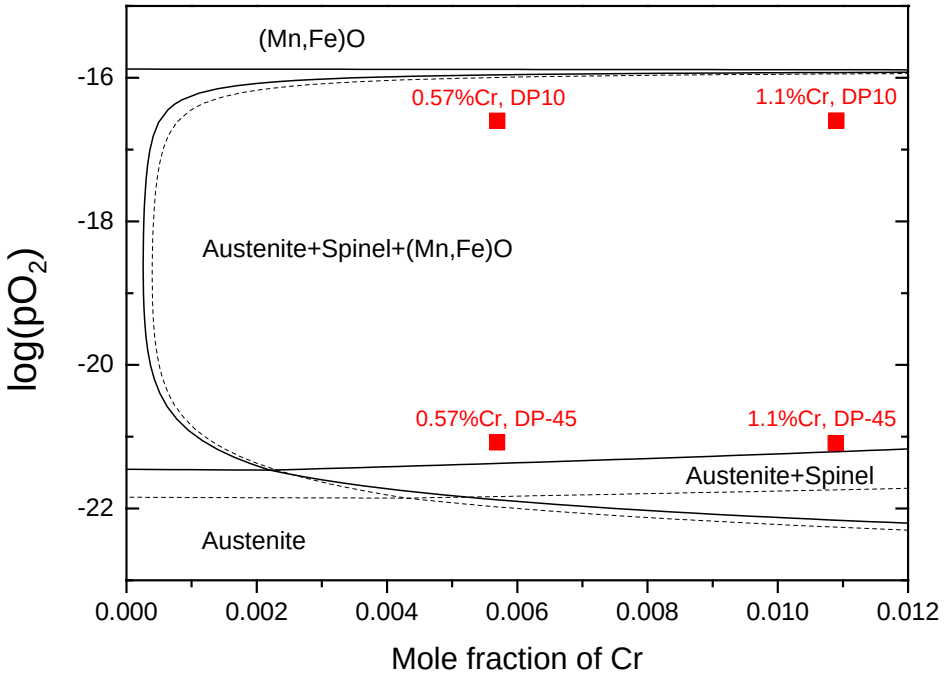

Figure 2.3 Phase diagrams of Fe-Mn-Cr alloys with Mn concentration fixed at 1.8 or 2.8 (dashed lines) mol.% at 950 °C in an O_2 environment computed with the thermodynamic tool "FactSage"[8].[23]

The type of oxides is a function of alloy composition and oxygen partial pressure. As shown in Figure 2.3, at very low oxygen partial pressure, say below 10^{-23} atm, steel remains austenite phase, no oxidation happened. As the pO_2 increase, selective oxidation of alloying elements occurs. Two types of oxides (Mn, Fe) O monoxide and Mn-Cr spinel oxide $MnCr_2O_4$ are found in the phase diagram. When the oxygen partial pressure further increased and reached the dissociation pO_2 of FeO (Wüstite), the formation of FeO is thermodynamically favorable and a Wüstite scale is expected.

When the Cr concentration is higher than 0.23 at. % (with Mn fixed at 1.8 at. %), with the increase of pO_2, the first formed oxide is Mn-Cr spinel oxide $MnCr_2O_4$ since the dissociation oxygen partial pressure of $MnCr_2O_4$ is first reached. The reaction of formation of Mn-Cr spinel oxide $MnCr_2O_4$ is[24, 25]:

$$Mn + 2Cr + 2O_2 = MnCr_2O_4 \qquad (2.31)$$

The dissociation oxygen partial pressure of Mn-Cr spinel oxide $MnCr_2O_4$ is defined as:

$$pO_2 = \left(\frac{a_{MnCr_2O_4}}{(a_{Cr})^2 a_{Mn}} \right) \exp\left(\frac{\Delta G^0_{f,MnCr_2O_4}}{2RT}\right) \quad (2.32)$$

The activity of alloying element Mn and Cr dissolved in the alloy depends on their concentrations. The dissociation pO_2 of $MnCr_2O_4$ is effect by the activity of Cr and Mn according to Eq. (2.31). With the increase of Cr concentration, the activity of Cr also increases leading to the decrease of the dissociation pO_2 of $MnCr_2O_4$ as shown in the phase diagram. If the pO_2 increase further and reaches the dissociation pO_2 of MnO (above the dissociation pO_2 of MnO line as shown in the phase diagram), MnO will be formed according to Eq. (2.32):

$$Mn + O = MnO \quad (2.33)$$

The dissociation oxygen partial pressure of MnO is defined as

$$pO_2 = \left(\frac{a_{MnO}}{a_{Mn}} \right)^2 \exp\left(\frac{2\Delta G^0_{f,MnO}}{RT}\right) \quad (2.34)$$

In this phase diagram, the concentration of manganese is fixed at 1.8 at. %. With the increase of Cr concentration, the remaining dissolved Mn (not in form of Mn-Cr spinel oxides) decreases which leads to the decreases of activity of Mn. Thus, the dissociation pO_2 of MnO increases with the Cr concentration as shown in the phase diagram. When the Cr concentration is lower than 0.23 at. % (with Mn fixed at 1.8 at. %), with the increase of pO_2, the first formed oxide is MnO according to Eq. (2.33). Then $MnCr_2O_4$ starts to form as the pO_2 further increase.

When the Fe-Mn-Cr alloy composition is fixed with Mn at 1.8 at. % and Cr at 1.5 at. %, at dew point ranging from -30 °C (corresponding pO_2 around 10^{-21} atm) to +10 °C (corresponding pO_2 around 10^{-17} atm), the formation of both MnO and $MnCr_2O_4$ are thermodynamically favorable.

CHAPTER 3

EXPERIMENTAL METHODS

3.1 Chemical composition of tested Samples

The steel samples were designated as Fe-1.7Mn, Fe-1.9Mn-1.0Cr-0.1Si, Fe-1.8Mn-1.5Cr-0.1Si, Fe-1.7Mn-1.4Cr, Fe-1.8Mn-1.0Cr-0.5Si, Fe-1.8Mn-2.0Si. These samples were received from TATA Steel, Netherlands. The bulk chemical compositions were measured by an optical emission spectrometer. The bulk chemical compositions in both weight percent and atomic percent of the samples are listed in Table 3.1

Table 3.1. The chemical composition of alloys tested.

Steel samples	Composition wt. % **(at. %)**				
	C	Mn	Cr	Si	Al
Fe-1.7Mn	0.103 **(0.477)**	1.70 **(1.72)**	-	0.05 **(0.10)**	0.002 **(0.004)**
Fe-1.9Mn-1.0Cr-0.1Si	0.099 **(0.459)**	1.88 **(1.90)**	0.91 **(0.97)**	0.05 **(0.15)**	0.026 **(0.054)**
Fe-1.8Mn-1.5Cr-0.1Si	0.098 **(0.453)**	1.83 **(1.85)**	1.53 **(1.63)**	0.05 **(0.15)**	0.024 **(0.049)**
Fe-1.7Mn-1.4Cr	-	1.67 **(1.70)**	1.39 **(1.49)**	<0.01	<0.05
Fe-1.8Mn-1.0Cr-0.5Si	0.101 **(0.47)**	1.80 **(1.82)**	1.02 **(1.09)**	0.26 **(0.51)**	0.019 **(0.039)**
Fe-1.8Mn-2.0Si	0.104 **(0.48)**	1.90 **(1.91)**	-	0.94 **(1.84)**	0.017 **(0.030)**

3.2 Isothermal Oxidation Experiments

Selective oxidation experiments were carried out at 950 °C on a series of Fe-Mn-Cr alloys with different alloying element compositions for 1,4,16 hours at -45, −30, -10,

+10 °C dew points (Ar + 5 vol.% H_2), respectively. The annealing conditions of selective oxidation experiments are listed in Appendix B.

The hot rolled steel ingots were cut into rectangular shaped species 20 mm × 10 mm ×1 mm in size. Prior to isothermal oxidation experiments, all the sample surfaces were mechanically ground with grinding paper from P400 to P4000, followed by mechanically polishing with 1 μm diamond paste. Before each step, all samples were ultrasonically cleaned in ethanol for 5 mins and rapidly dried by air gun with a flow of nitrogen.

The oxidizing atmosphere was the gas mixtures of argon and hydrogen Ar/H_2 (95/5 v/v) with humidity of -45, -30, -10, +10 °C dew points, separately. As the saturated pressure of water vapor is the function of dew point (DP)[26] according to Appendix A. Evaporated pure water (18.2 MΩ.cm at 25 °C) was added to the gas mixture with a CEM (Controlled Evaporator Mixer) to create certain dew point. The dew point was monitored, for low dew point -30 °C and -45 °C, by cooled mirror analyzer (S4000 TRS, Michell Instrument, UK). The fluctuation of dew points during oxidation experiments was within ±2 °C.

A quartz tube with a diameter of 30 mm is placed in a horizontal tube furnace. The specimens were placed horizontally on a boat shaped quartz holder and inserted into the hot zone of the furnace by a quartz rod once the temperature of 950 °C was reached. The samples were positioned parallel to the direction of gas flow. The temperature at the position of the specimen was measured by the thermocouple which was located near the specimen inside the furnace. Prior to the oxidation experiment, a dry pure argon gas flow was kept flushing through the quartz tube. After the oxidation experiment, samples were pulled back to the cold zone of the quartz tube, and immediately switch the gas from $Ar/H_2/H_2O$ to pure Ar.

3.3 Reduction of external oxides

A series of experiments on the first oxidation and subsequent reduction on three samples with different alloying composition were carried out. These samples were first oxidized at 950 °C in Ar plus 5 vol.% H_2 gas mixtures with -30°C dew point for 1h and then reduced at 950 °C in dry Ar + 5 vol% H_2 gas mixture for 1h. The samples after annealing were stored in an airtight membrane box. The annealing conditions are listed in Table 3.2.

Table 3.2. Annealing conditions of selective oxidation and subsequent reduction experiments

Steel ingots	**Oxidation Temperature (°C)**	**Oxidation Time (hour)**	**Dew point (°C)**	**Reduction Temperature (°C)**	**Reduction Time (hour)**	**Reduction atmosphere**
Fe-1.7Mn-1.4Cr	950	1	-30	950	1	Ar+5vol.% H_2
Fe-1.8Mn-1.5Cr-0.1Si	950	1	-30	950	1	Ar+5vol.% H_2
Fe-1.8Mn-1.0Cr-0.5Si	950	1	-30	950	1	Ar+5vol.% H_2

A series of Wüstite formation and reduction experiments were carried out. The samples were first oxidized at 950 °C in Ar+ 33 vol.% CO_2+ 17 vol.% CO gas mixture for 4h and then reduced at 950 °C in Ar+5vol.% H_2 gas mixture for 2h. The annealed samples were stored in an airtight membrane box. The annealing conditions are listed in Table 3.3.

Table 3.3. Annealing conditions of Wüstite formation and reduction

Steel ingots	**Oxidation Temperature (°C)**	**Oxidation Time (hour)**	**Oxidation atmosphere**	**Reduction Temperature (°C)**	**Reduction Time (hour)**	**Reduction atmosphere**
Fe-1.7Mn-1.4Cr	950	4	Ar+33vol.%CO_2+17vol.% CO	950	2	Ar+5vol.% H_2
Fe-1.8Mn-1.5Cr-0.1Si	950	4	Ar+33vol.%CO_2+17vol.% CO	950	2	Ar+5vol.% H_2

Fe-1.8Mn-1.0Cr-0.5Si	950	4	Ar+33vol.%CO_2+17vol.% CO	950	2	Ar+5vol.% H_2
Fe-1.8Mn-2.0Si	950	4	Ar+33vol.%CO_2+17vol.% CO	950	2	Ar+5vol.% H_2

3.4 Characterization Methods

3.4.1 Scanning electron microscopy (SEM) and X-ray microanalysis (XMA)

The morphology and chemical composition of the oxidized samples were investigated by Field-Emission Scanning Electron Microscope (JEOL, JSM-6500F, Japan) equipped with an energy-dispersive spectrometer (with a Noran System 7, USA).

The morphology of surface and cross-section of all oxidized samples were recorded by both secondary electron and backscattered electron images. Surface observation is operating at an accelerating voltage of 5 kV and a working distance of 10 mm. Cross-section observation is operating at an accelerating voltage of 15 kV and a working distance of 10 mm. During cross-section preparation, a Cu layer of about 1 μm was deposited on the surface by a high vacuum sputter coater (Leica, EM SCD500, Germany) to preserve the oxidized samples and identify surface of sample clearly. Then the sample was glued to a silicon wafer with epoxy resin (G2 epoxy resin, Gatan 601.07270, UK). All the sample surfaces were mechanically ground with grinding paper from P400 to P2500, followed by mechanically polishing from 3 μm to 0.25 μm diamond paste. Before each step, all samples were ultrasonically cleaned in ethanol for 5 mins and rapidly dried by a flow of nitrogen.

The chemical composition of all oxidized samples was determined by X-ray microanalysis using Electron Dispersive Spectroscopy (EDS) operating at an accelerating voltage of 10 kV and a working distance of 25 mm.

3.4.2 Electron probe X-ray microanalysis (EPMA)

Electron probe X-ray microanalysis (EPMA) was used to determine the concentration of the alloying elements and oxygen. The oxidized samples were analyzed using a

microprobe (JEOL JXA 8900R, Japan) employing by Wavelength Dispersive Spectrometry (WDS). The energy of the electron beam and beam current were 10 keV and 50 nA. To obtain the concentration depth profiles of alloying elements and oxygen, an average concentration at each depth was obtained from 40 analyzed points parallel to the sample surface. The distance between the parallel lines was 1 μm. To obtain the dissolved concentration of Cr in the IOZ, points for analysis were handpicked to be in-between the oxide precipitates.

3.4.3 Image analysis

The volume fraction of internal oxide precipitates was determined from the backscattered electron images of cross-sections prepared from the oxidized samples. The images were converted into binary images and analyzed with image processing program Image J. By counting the black pixels (internal oxides) and white pixels (matrix), the volume fractions of internal oxide precipitates can be obtained.

3.4.4 X-ray diffraction (XRD)

To identify the type of oxides formed on the surfaces of all oxidized samples, X-ray diffraction patterns were recorded with a Bruker D8 (Germany) advance diffractometer equipped with a Vantec position sensitive detector and graphite monochromator in the Bragg-Brentano geometry. The XRD measurements were carried out at room temperature using Co-Kα radiation source with wavelength 0.179026 nm. The Coupled θ -2θ scan was recorded from 10° to 110° with a step size 0.034 º (2θ) and the counting time is per step 4 s. The samples were spinning during the measurement. Data evaluation was done with the Bruker software Diffrac Suite. EVA vs 4.2. The measured X-ray diffraction patterns were analyzed after background subtraction.

3.4.5 Lattice parameter determination

To study the iron dissolution in $MnCr_2O_4$ spinel, the measurement of lattice constant of $MnCr_2O_4$ spinel on samples Fe-1.8Mn-1.5Cr-0.1Si alloys annealed at 950°C in Ar

plus 5 vol.% H_2 gas mixture for 16 hours with dew points of -45 and 10 °C were carried out. The lattice parameters of oxides were determined from X-ray diffraction patterns. The residual stress of the spinel oxide film was measured for the {440} reflections and that for the iron was measured for the {211} reflections. The XRD patterns at various tilting angles (psi), d-$\sin^2$psi and a-$\sin^2$psi plots are recorded by Bruker D8 Discover with a Eulerian cradle with parallel beam geometry. The XRD measurements were carried out at room temperature using Co-Kα radiation source with wavelength 0.179026 nm. The scan voltage is 45 kV and scans current is 25 mA. The coupled θ-2θ scan for spinel {440} was recorded from 72° to 77° with a step size 0.02 ° (2θ) and the counting time is per step 30 s. The coupled θ-2θ scan for Fe {211}was recorded from 98° to 102° with a step size 0.02 ° (2θ) and the counting time is per step 2 s. In the residual stress analysis, Kα2 was stripped, the peak shape was fitted with a modified Lorentzian profile.

CHAPTER 4

RESULTS AND DISCUSSION

4.1 Identification of oxide phases

Figure 4.1 shows the X-ray diffraction pattern of Fe-1.7Mn-1.4Cr alloys annealed at 950°C in Ar plus 5 vol.% H_2 gas mixture for 16 hours with dew points of -30 °C. Figure 4.2 shows the X-ray diffraction patterns of Fe-1.8Mn-1.5Cr-0.1Si alloys annealed at 950°C in Ar plus 5 vol.% H_2 gas mixture for 1 hour with dew points of -30, -10, 10 °C. According to the X-ray diffraction patterns, the identified oxide phases for all samples are A: $(Cr,Mn,Fe)_3O_4$ spinel (blue pattern) and B: (Mn,Fe)O (green pattern). The Cr_2O_3 phase is not identified in the X-ray diffraction patterns for all samples. The chemical composition of oxides determined by X-ray microanalysis using Electron Dispersive Spectroscopy (EDS) are shown in Appendix C. The EDS results suggest the oxide phases are $(Cr,Mn,Fe)_3O_4$ spinel and (Mn,Fe)O. The identified oxide species formed during annealing Fe-Mn-Cr steel alloys are in good agreement with the prediction with the thermodynamic tool “FactSage”.

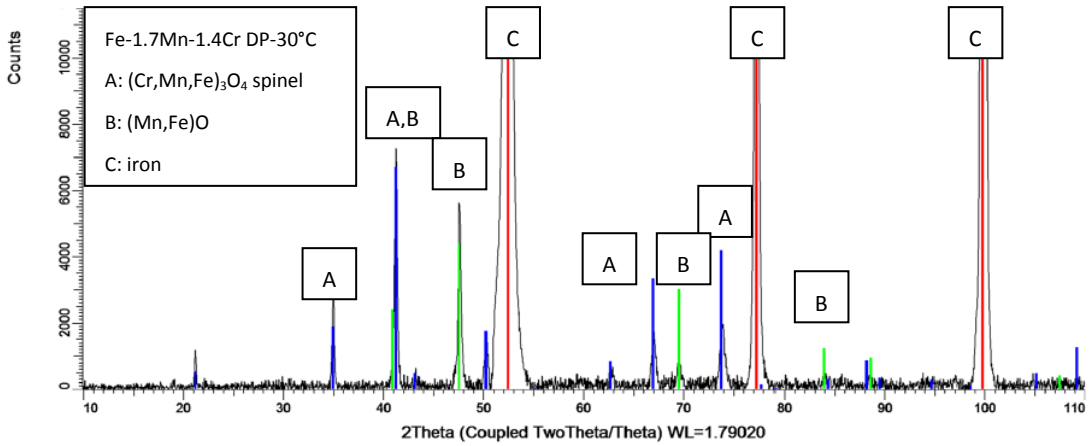

Figure 4.1 X-ray diffraction pattern of Fe-1.7Mn-1.4Cr alloys annealed at 950°C in Ar plus 5 vol.% H_2 gas mixture for 16 hours with a dew point of -30 °C.

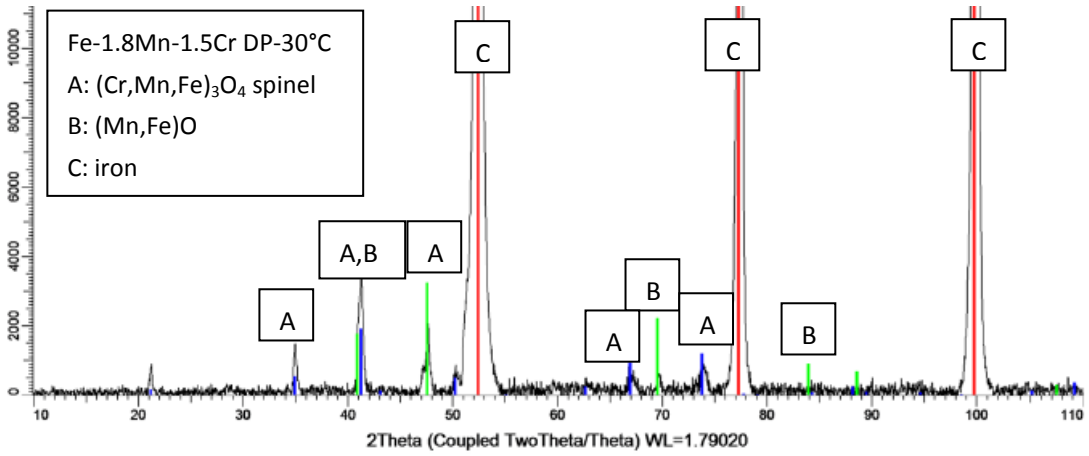

(a)

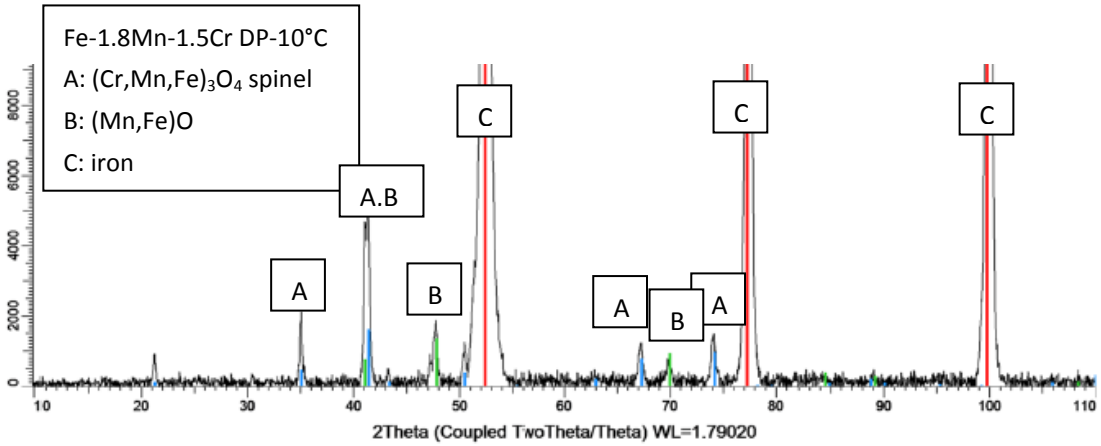

(b)

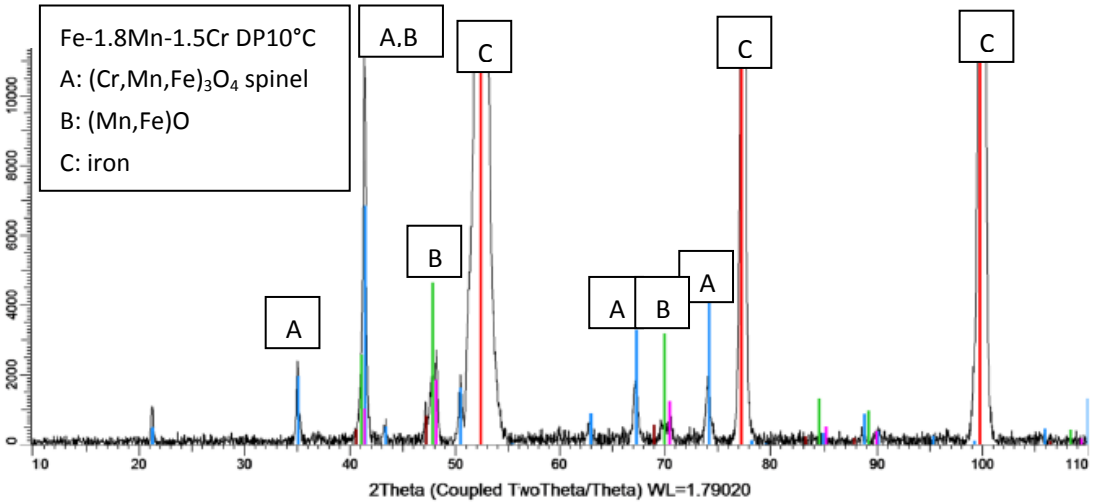

(c)

Figure 4.2 X-ray diffraction patterns of Fe-1.8Mn-1.5Cr-0.1Si alloys annealed at 950°C in Ar plus 5 vol.% H_2 gas mixture for 1 hour with dew points of -30, -10, 10 °C, respectively.

4.2 Dissolution of iron in oxides

The dissolution of iron in MnO and $MnCr_2O_4$ to form (Mn,Fe)O and $(Mn,Cr,Fe)_3O_4$ oxide solid solution is predicted with the thermodynamic tool "FactSage". The Fe concentration dissolved in (Mn,Fe)O and $(Mn,Cr,Fe)_3O_4$ increases with oxygen partial pressure is predicted. In the previous study [14], it is already proved that iron is dissolved in MnO and the Fe concentration in (Mn,Fe)O increases with dew point during annealing of Fe-Mn binary steel alloys. The lattice constant of $MnCr_2O_4$ spinel on Fe-1.8Mn-1.5Cr-0.1Si alloys annealed at 950°C in Ar plus 5 vol.% H_2 gas mixture for 16 hours with dew points of -45 and 10 °C are measured to study iron dissolution in $MnCr_2O_4$ spinel and the results are shown in Table 4.1.

Table 4.1 Stress free lattice constants of Mn-Cr spinel in Fe-1.8Mn-1.5Cr-0.1Si steel alloys annealed at 950°C in Ar plus 5 vol.% H_2 gas mixture for 16 hours with dew points of -45 and 10 °C.

Sample Phase hkl	Residual stress	Residual strain	d_0	a_0
	(MPa)	(ppm)	(Å)	(Å)
1.5Mn1.5Cr_DP-45				
Fe {211}	15±5	74±23	1.1708	2.8678±0.0001
(Fe,Mn,Cr)3O4 {440}	-266±68	-2085±531	1.4904	8.4310±0.0015
1.5Mn1.5Cr_DP10				
Fe {211}	54±11	273±5	1.1703	2.8666±0.0001
(Fe,Mn,Cr)3O4 {440}	-7±6	-51±50	1.4872	8.4133±0.0005

The measured stress free lattice constants of Mn-Cr spinel in Fe-1.8Mn-1.5Cr-0.1Si steel alloys annealed at 950 °C in Ar plus 5 vol.% H_2 gas mixture for 16 hours with dew points of -45 and 10 °C are (8.4310±0.0015) Å and (8.4133±0.0005) Å, respectively.

Iron dissolution in spinel changes lattice constant of spinel [27,28]. According to the standard PDF cards in Appendix D, the lattice constant of $MnCr_2O_4$ spinel is around 8.43325 Å. The measured lattice constant of spinel formed at DP -45 and 10 °C are different from standard PDF cards. Therefore, iron is dissolved in $MnCr_2O_4$ spinel at our annealing condition. Measurement is in agreement with the prediction with the thermodynamic computation.

Iron can substitute both manganese at A-site (8a site, tetragonal) and chromium at B-site (16d site, octahedral). If iron substituted at A- site in Mn-Cr spinel (AB_2O_4), the lattice parameter will decrease. While if iron substituted at B- site in Mn-Cr spinel, the lattice parameter will increase. The lattice constants of $FeCr_2O_4$ and $MnFe_2O_4$ in standard PDF cards are around 8.37776 Å and 8.50547 Å, respectively (see Appendix D). Figure 4.3 [28] shows the lattice constant of $Mn_{1-x}Fe_xCr_{2-y}Fe_yO_4$ at room temperature as a function of iron content. Since ferrous (Fe^{2+}) is thermodynamically favorable compared to ferric (Fe^{3+}) at our annealing condition, iron ions are mainly substituted Mn ions. Therefore, the lattice constant of Mn-Cr spinel at our annealing condition decreases with increasing iron content.

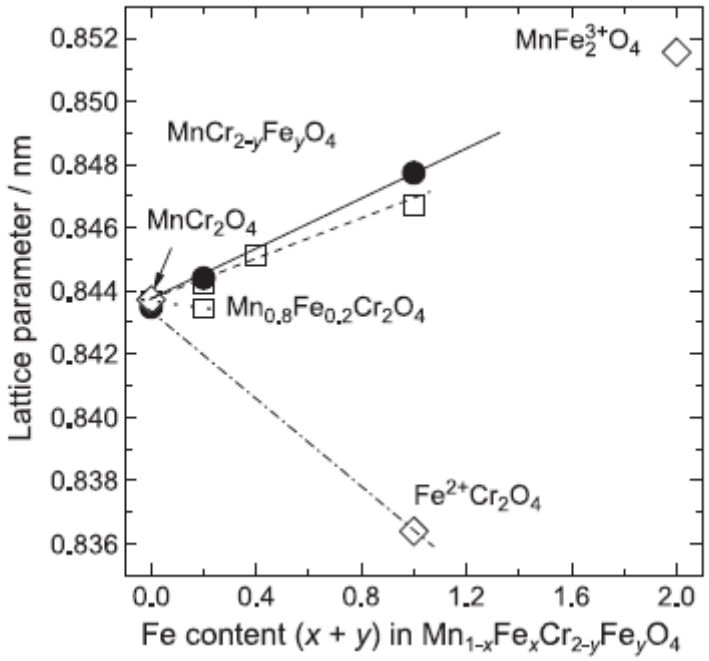

Figure 4.3 Lattice constant of $Mn_{1-x}Fe_xCr_{2-y}Fe_yO_4$ at room temperature as a function of iron content. [28]

The measured stress free lattice constant of Mn-Cr spinel formed at DP -45 °C is bigger than that of Mn-Cr spinel formed at DP 10 °C. The measured lattice constant of Mn-Cr spinel decreases with annealing dew point. This indicates that the Fe concentration in $(Mn,Cr,Fe)_3O_4$ increases with annealing dew point. Therefore, measurement is in agreement with expectation.

4.3 Coverage of oxides at steel surface

4.3.1 Effect of dew point on coverage of oxides at steel surface

Figure 4.4 shows the backscattered electron images of the surfaces of Fe-1.8Mn-1.5Cr-0.1Si alloys annealed at 950°C in Ar plus 5 vol.% H_2 gas mixture for 1 hour with dew points of -45 (a), -30 (b), -10 (c) and 10 (d) °C.

At -45 °C dew point (see Figure 4.4 (a)), the sample surface is not fully covered by oxides and the coverage of oxides at steel surface by image analysis is about 14 to 17 %. Oxides at steel surface are distributed both at grain boundary and inside grain. The size of oxides at grain boundary is larger than inside grain.

At -30 °C dew point (see Figure 4.4 (b)), the sample surface is not fully covered by oxides and the coverage of oxides at steel surface by image analysis ranged from 20 to 27%. Oxides at steel surface formed at grain boundary and inside grain cannot be distinguished clearly.

At -10 °C dew point (see Figure 4.4 (c)), the sample surface is not fully covered by oxides and the coverage of oxides at steel surface by image analysis ranged from 24 to 29%. Oxides at steel surface are distributed both at grain boundary and inside grain. The size of oxides at grain boundary is larger than inside grain.

At 10 °C dew point (see Figure 4.4 (d)), the sample surface is not fully covered by oxides and the coverage of oxides at steel surface by image analysis ranged from 21 to 28%. Oxides at steel surface formed at grain boundary and inside grain cannot be distinguished clearly.

The surfaces of Fe-1.8Mn-1.5Cr-0.1Si alloys annealed at 950 °C in Ar plus 5 vol.% H_2 gas mixture for 1 hour with four dew points are all not fully covered by oxides. Coverage of oxides at steel surface does not change significantly with dew point.

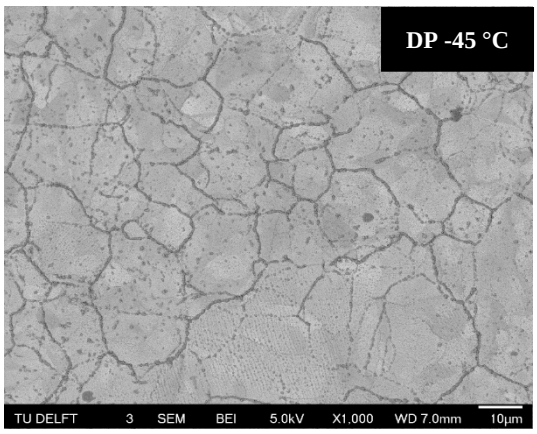

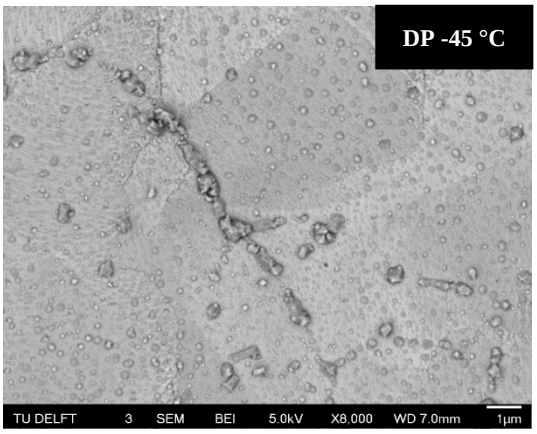

(a)

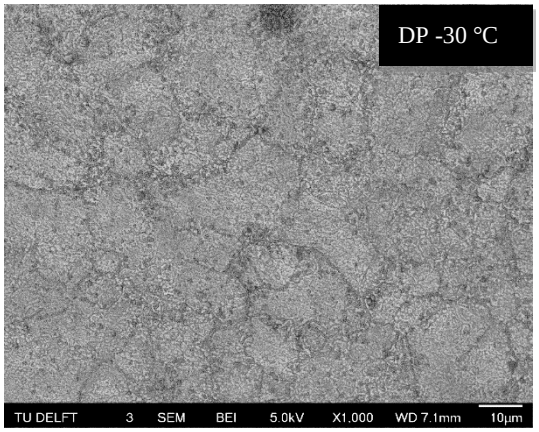

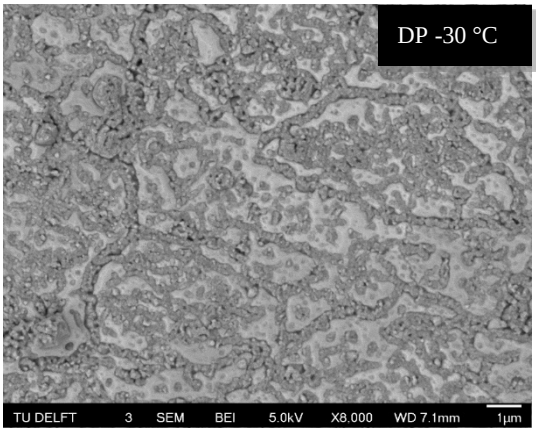

(b)

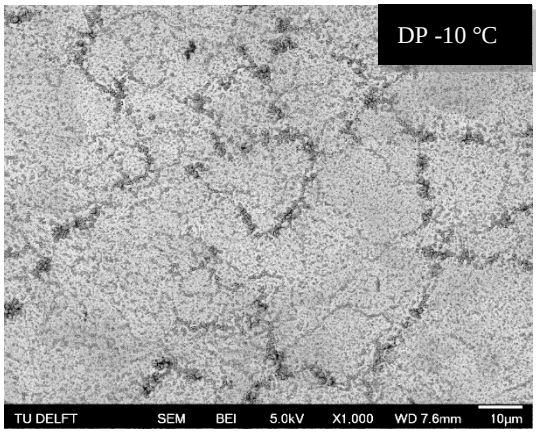

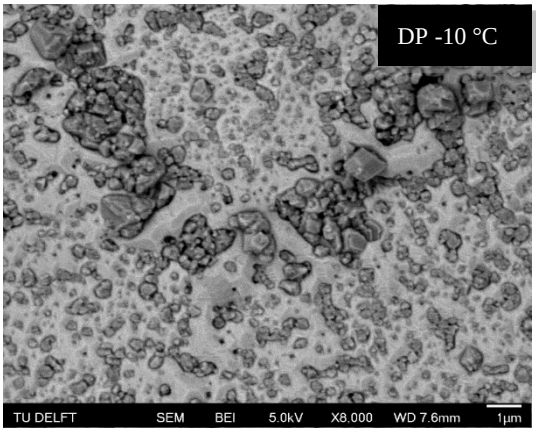

(c)

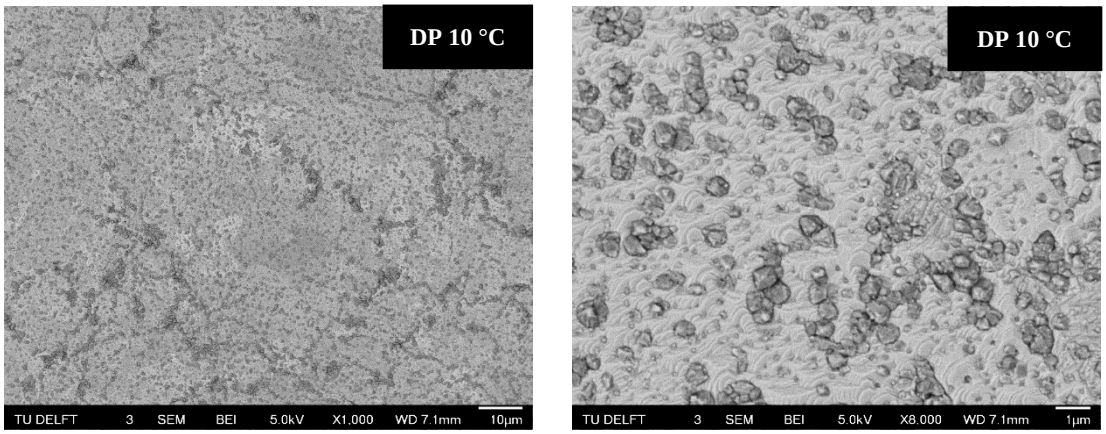

(d)

Figure 4.4 Backscattered electron images of the surface of Fe-1.8Mn-1.5Cr-0.1Si steel alloys annealed at 950°C in Ar plus 5 vol.% H_2 gas mixture for 1 hour with dew points of -45 (a), -30 (b), -10 (c) and 10 (d) °C.

4.3.2 Effect of oxidation time on coverage of oxides at steel surface

Figure 4.5 shows the backscattered electron images of the surfaces of Fe-1.8Mn-1.5Cr-0.1Si steel alloys annealed at 950°C in Ar plus 5 vol.% H_2 gas mixture for 1 and 16 hours with dew points of -45 (a), -30 (b), -10 (c) and 10 (d) °C.

For samples of Fe-1.8Mn-1.5Cr-0.1Si steel alloys annealed at 950 °C in Ar plus 5 vol.% H_2 gas mixture with a dew point of -45 °C (see Figure 4.5 (a)), the surfaces are not fully covered with oxides with increasing oxidation time. The coverage of oxides at steel surface of samples annealed 1 hour and 16 hours is about 14% to 17% and 40% to 52%, respectively. Coverage of oxides at steel surface increases with oxidation time at dew point -45 °C.

For samples of Fe-1.8Mn-1.5Cr-0.1Si steel alloys annealed at 950 °C in Ar plus 5 vol.% H_2 gas mixture with dew points of -30, -10, 10 °C (see Figure 4.5 (b)(c)(d)), the surfaces are not fully covered with oxides with increasing oxidation time. The coverage of oxides at steel surface does not change significantly with oxidation time.

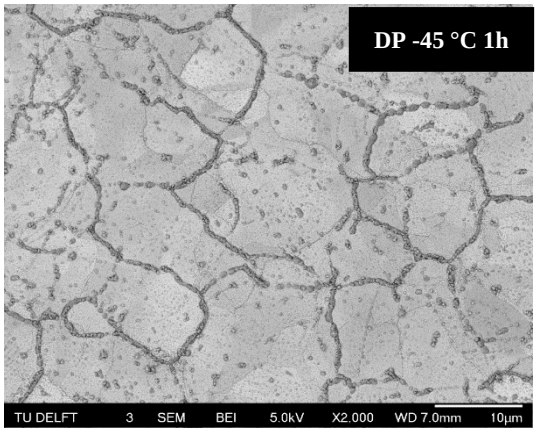
DP -45 °C 1h
TU DELFT 3 SEM BEI 5.0kV X2,000 WD 7.0mm 10µm

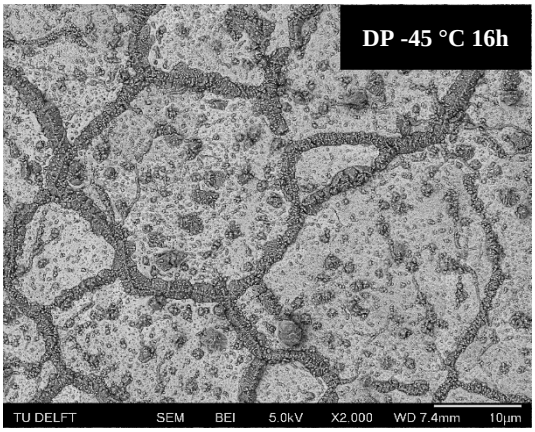
DP -45 °C 16h
TU DELFT SEM BEI 5.0kV X2,000 WD 7.4mm 10µm

(a)

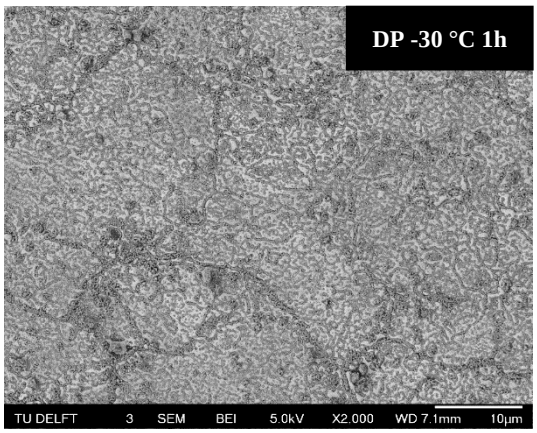
DP -30 °C 1h
TU DELFT 3 SEM BEI 5.0kV X2,000 WD 7.1mm 10µm

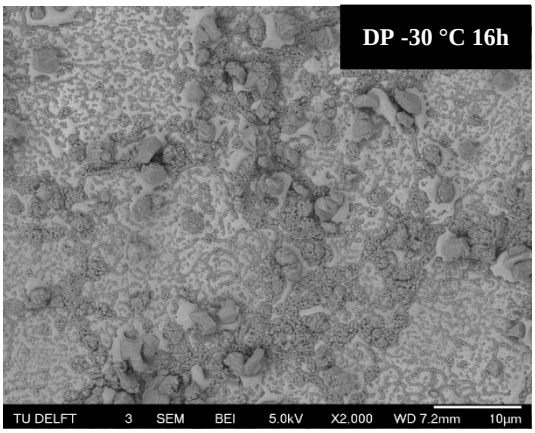
DP -30 °C 16h
TU DELFT 3 SEM BEI 5.0kV X2,000 WD 7.2mm 10µm

(b)

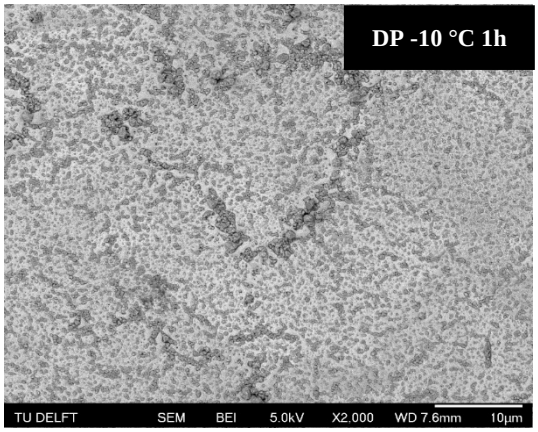
DP -10 °C 1h
TU DELFT SEM BEI 5.0kV X2,000 WD 7.6mm 10µm

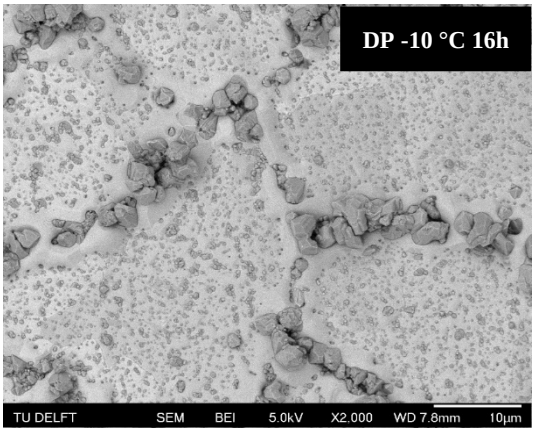
DP -10 °C 16h
TU DELFT SEM BEI 5.0kV X2,000 WD 7.8mm 10µm

(c)

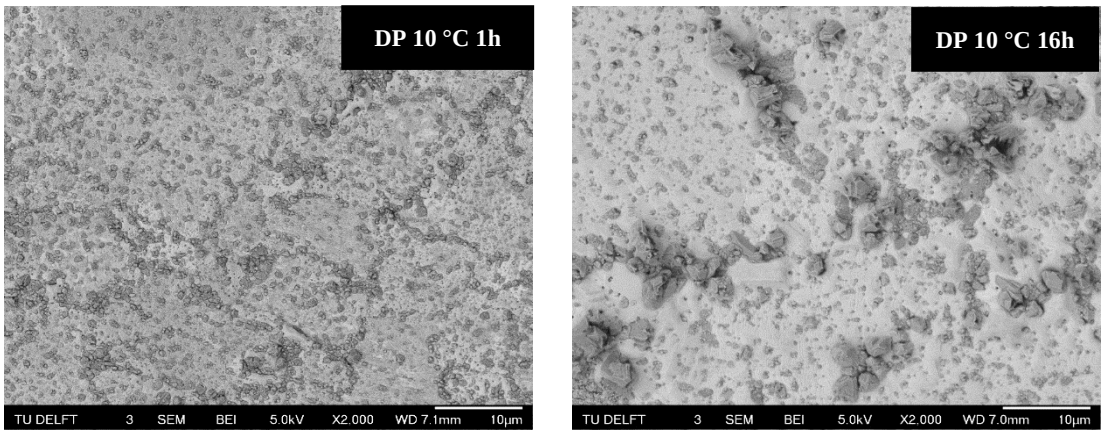

(d)

Figure 4.5 Backscattered electron images of the surfaces of Fe-1.8Mn-1.5Cr-0.1Si alloys annealed at 950°C in Ar plus 5 vol.% H_2 gas mixture for 1 and 16 hours with dew points of -45 (a), -30 (b), -10 (c) and 10 (d) °C.

4.4 Transition from external to internal oxidation

The variation of dew point affects the oxidation mode. According to Wagner model, as described in section 2.1, increasing dew points promoted the internal oxidation. In this section, the Fe-1.8Mn-1.5Cr-0.1Si steel alloys annealed at 950°C in Ar plus 5 vol.% H_2 gas mixture for 1 and 16 hours with four dew points of -45, -30, -10 and 10 °C are discussed.

Figure 4.6 (a) shows cross sections of Fe-1.8Mn-1.5Cr-0.1Si alloys annealed at 950°C in Ar plus 5 vol.% H_2 gas mixture for 1 hour with a dew point of -45 °C. The oxides formed at steel surface are observed but not continuous. Internal oxidation zone is not observed in the cross-section area. Increasing the oxidation time to 16 hours (see Figure 4.6(b)), the oxides formed at steel surface are observed but still not continuous. Internal oxides are mainly precipitated along the grain boundary. Internal oxidation zone inside grain is still not observed in the cross-section area. Therefore, the oxidation mode for Fe-1.8Mn-1.5Cr-0.1Si alloys annealed at 950°C in Ar plus 5 vol.% H_2 gas mixture with a dew point of -45 °C is external oxidation mode.

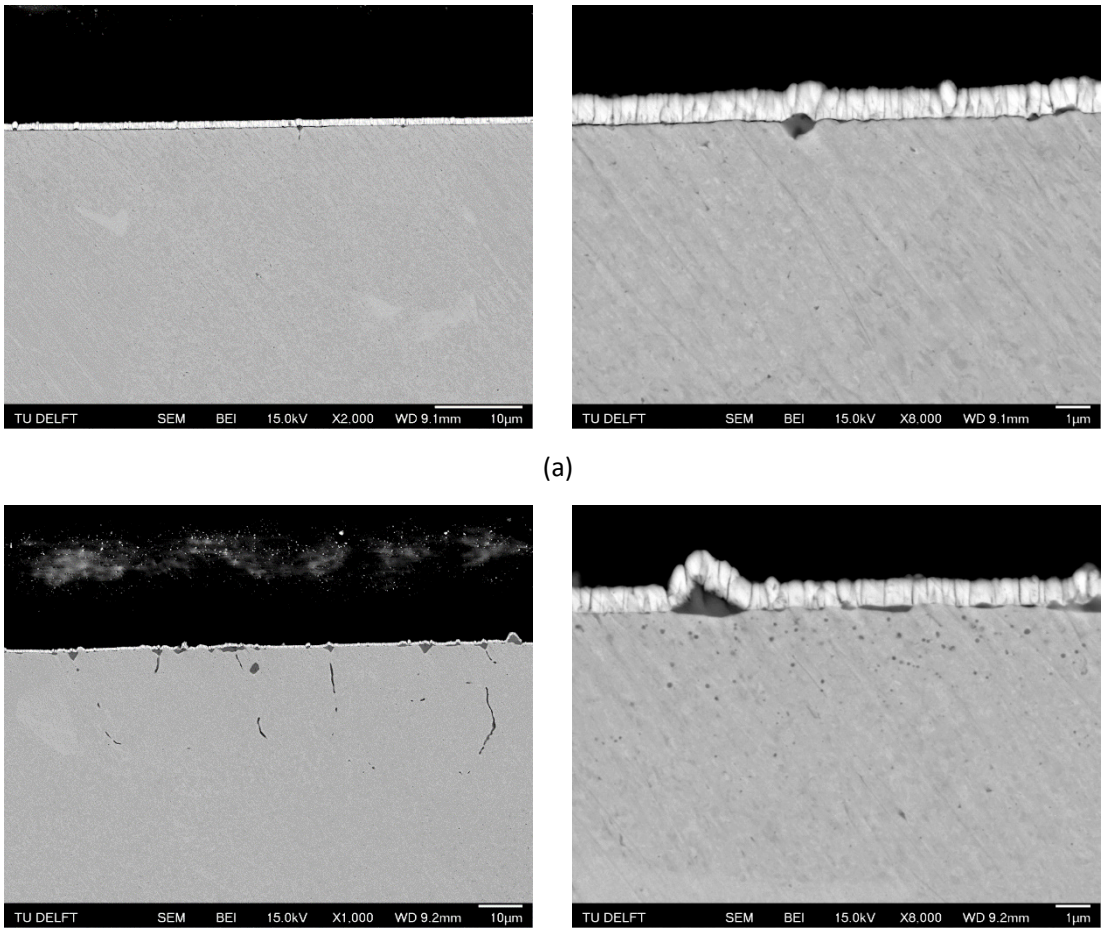

Figure 4.6 Backscattered electron images of the cross-section of Fe-1.8Mn-1.5Cr-0.1Si steel alloys annealed at 950°C in Ar plus 5 vol.% H_2 gas mixture for 1 hour (a) and 16 hours (b) with dew points of -45°C.

Figure 4.7 shows cross sections of Fe-1.8Mn-1.5Cr-0.1Si alloys annealed at 950°C in Ar plus 5 vol.% H_2 gas mixture for 1, 4, 16 hours with a dew point of -30 °C. The microstructure apparently shows that internal oxidation and external oxidation occur simultaneously. The external oxides are observed on the surface. Internal oxides are formed and the size of internal oxidation zone increases with oxidation time. Internal oxides are also formed along the grain boundary. These results indicated that the transition from external oxidation to internal oxidation occurred on Fe-1.8Mn-1.5Cr-0.1Si alloys annealed at 950°C in Ar plus 5 vol.% H_2 gas mixture with a dew point of -30 °C.

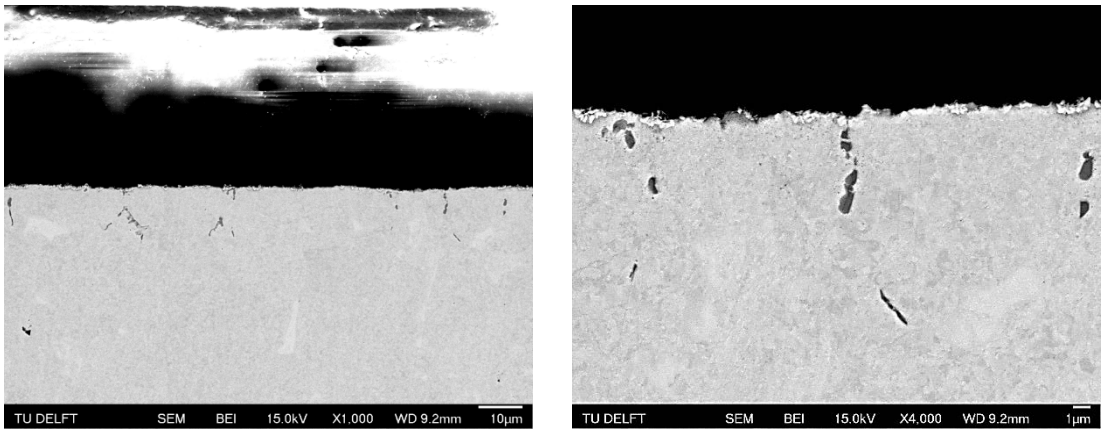

(a)

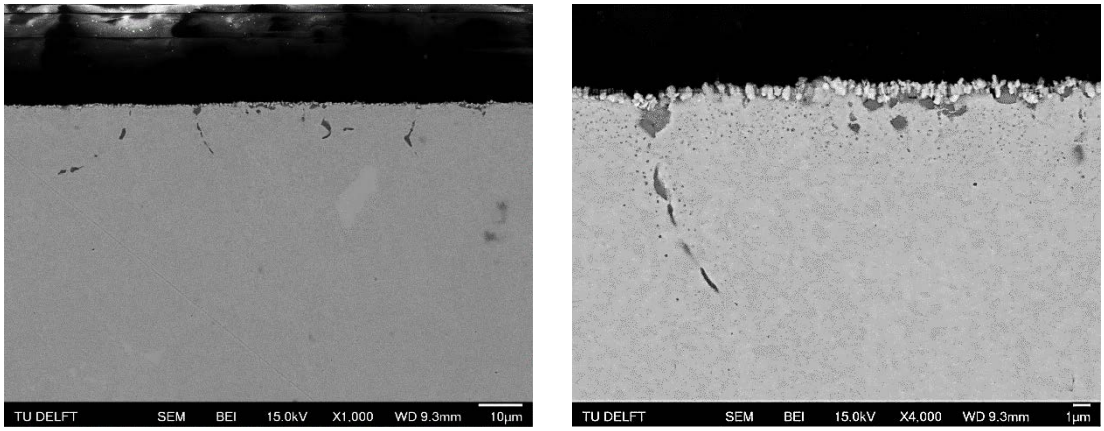

(b)

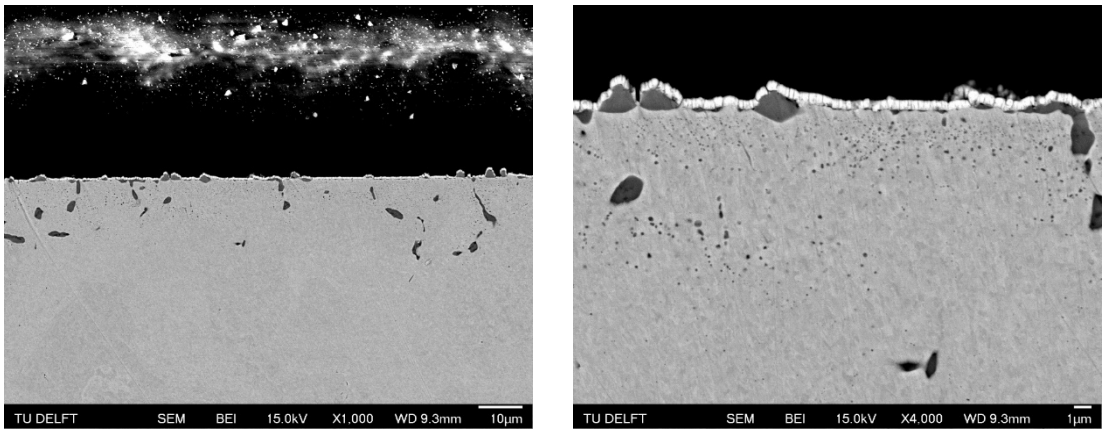

(c)

Figure 4.7 Backscattered electron images of the cross-section of Fe-1.8Mn-1.5Cr-0.1Si steel alloys annealed at 950°C in Ar plus 5 vol.% H_2 gas mixture for 1 hour (a),4 hours (b) and 16 hours (c) with a dew point of -30°C.

The Fe-1.8Mn-1.5Cr-0.1Si alloys annealed at 950°C in Ar plus 5 vol.% H_2 gas mixture with dew points higher than -10 °C is internally oxidized. Figure 4.8 shows cross sections of Fe-1.8Mn-1.5Cr-0.1Si alloys annealed at 950°C in Ar plus 5 vol.%

H_2 gas mixture for 1 hour and 16 hours with a dew point of -10 °C. Figure 4.9 shows cross sections of Fe-1.8Mn-1.5Cr-0.1Si alloys annealed at 950°C in Ar plus 5 vol.% H_2 gas mixture for 1 hour and 16 hours with a dew point of 10 °C. Internal oxides are formed both along the grain boundary and inside grain. A clear internal oxidation zone is observed and internal oxidation zone is increased with oxidation time. The average internal oxidation depth for sample annealed for 16 hours with -10 °C dew point is about 8.5±0.3 micron and that for sample annealed for 16 hours with 10 °C dew point is about 18.9±1 micron.

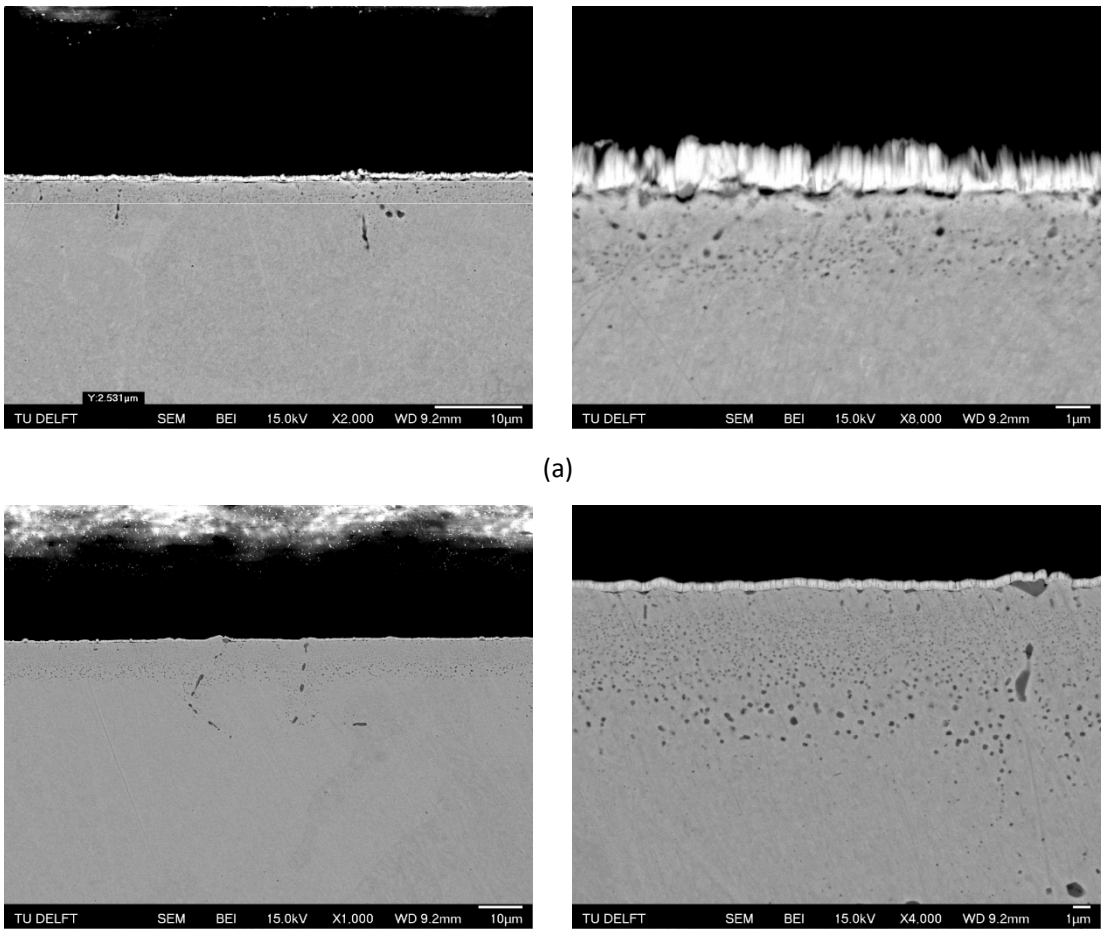

Figure 4.8 Backscattered electron images of the cross-section of Fe-1.8Mn-1.5Cr-0.1Si steel alloys annealed at 950°C in Ar plus 5 vol.% H_2 gas mixture for 1 hour (a) and 16 hours (b) with a dew point of -10°C.

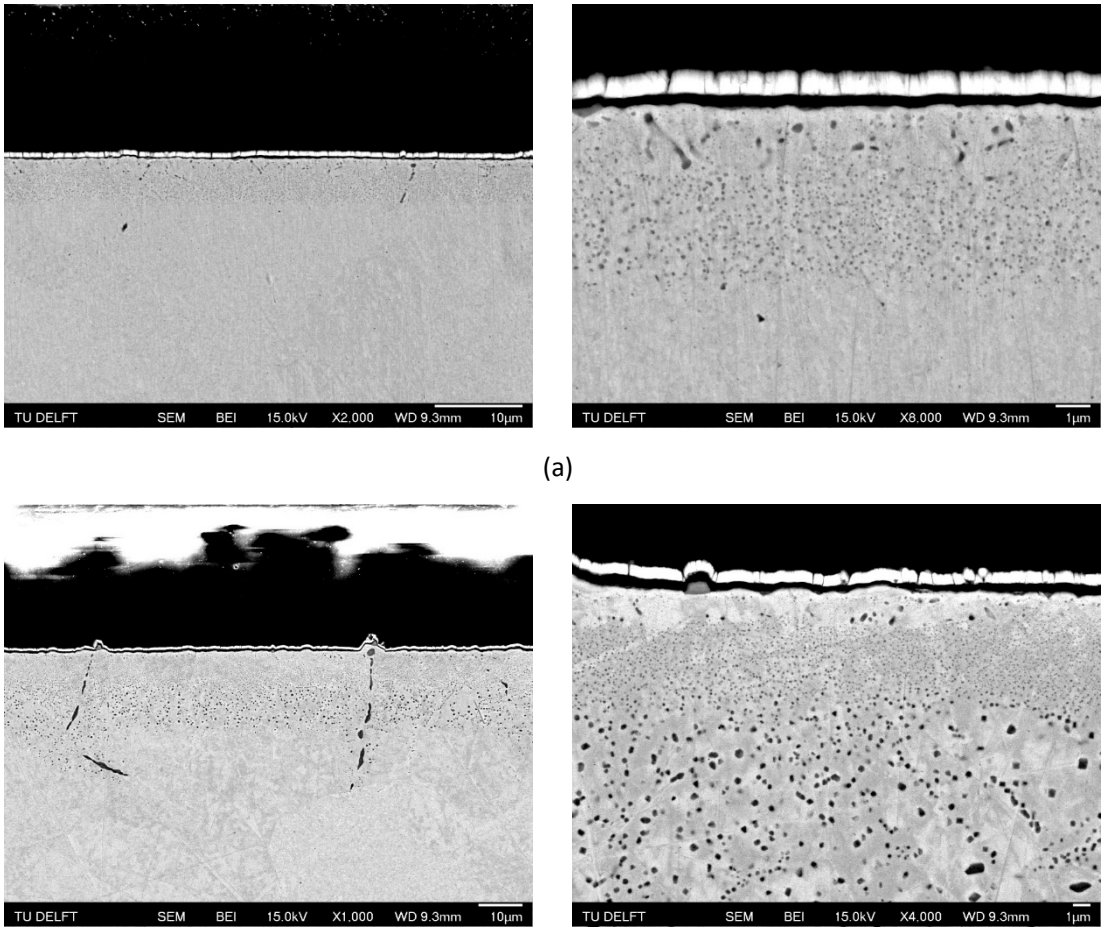

Figure 4.9 Backscattered electron images of the cross-section of Fe-1.8Mn-1.5Cr-0.1Si steel alloys annealed at 950°C in Ar plus 5 vol.% H_2 gas mixture for 1 hour (a) and 16 hours (b) with a dew point of 10°C.

4.5 Effect of Si on oxides formation along grain boundary

Figure 4.10 shows the backscattered electron images of the cross-section of Fe-1.7Mn-1.4Cr (without Si) and Fe-1.8Mn-1.5Cr-0.1Si alloys annealed at 950°C in Ar plus 5 vol.% H_2 gas mixture for 16 hours with a dew point of -30°C. There are no grain boundary oxides observed in samples of Fe-1.7Mn-1.4Cr (without Si) while a lot of internal oxides are observed along the grain boundary in samples of Fe-1.8Mn-1.5Cr-0.1Si steel alloy.

The grain size of Fe-1.7Mn-1.4Cr alloy is around 3 times larger than Fe-1.8Mn-1.5Cr-0.1Si steel alloy (see Figure 4.11). That means the number of grain

boundary in Fe-1.7Mn-1.4Cr alloy is lower than Fe-1.8Mn-1.5Cr-0.1Si steel alloy. However, after observation of the whole cross section area of the oxidized Fe-1.7Mn-1.4Cr sample, there is still no grain boundary oxides observed. Therefore, Si promoted the formation of internal oxides along the grain boundary.

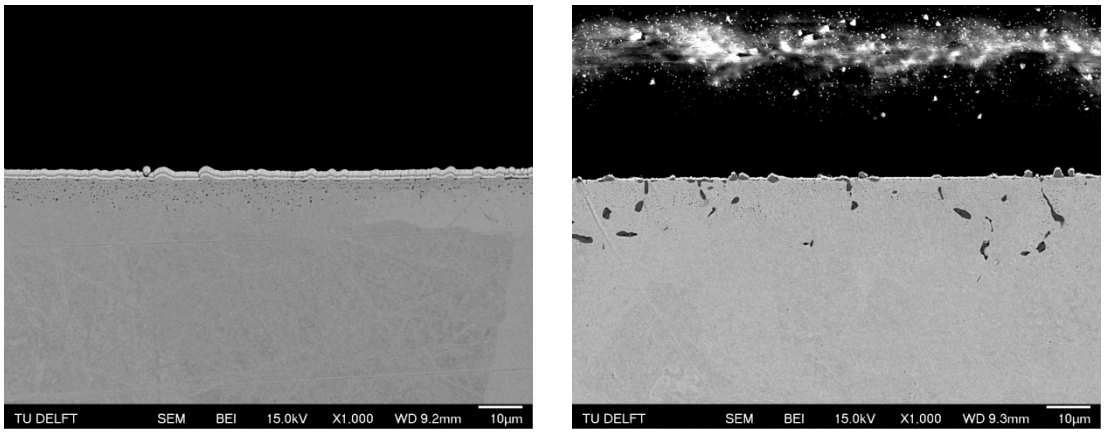

Fe-1.7Mn-1.4Cr (without Si) Fe-1.8Mn-1.5Cr-0.1Si

Figure 4.10 Backscattered electron images of the cross-section of Fe-1.7Mn-1.4Cr and Fe-1.8Mn-1.5Cr-0.1Si steel alloys annealed at 950°C in Ar plus 5 vol.% H_2 gas mixture for 16 hours with a dew point of -30°C.

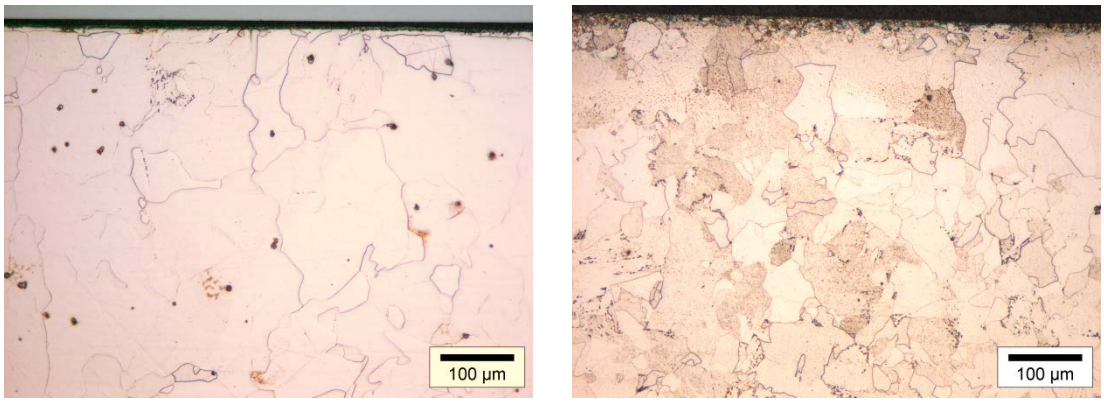

Fe-1.7Mn-1.4Cr (without Si) Fe-1.8Mn-1.5Cr-0.1Si

Figure 4.11 Optical microscope images of the cross-section of etched Fe-1.7Mn-1.4Cr and Fe-1.8Mn-1.5Cr-0.1Si steel alloys annealed at 950°C in Ar plus 5 vol.% H_2 gas mixture for 16 hours with a dew point of -30°C.

4.6 Kinetics of internal oxidation of Fe-Mn-Cr steel alloy

4.6.1 Effect of dew point on parabolic growth rate of IOZ

As discussed in chapter 2, with the assumption that the internal oxidation of Mn and Cr in the Fe-Mn-Cr alloys is a diffusion-controlled process, it is expected that the kinetics of internal oxidation obey a parabolic growth rate law. The depth of internal oxidation zone of Fe-1.8Mn-1.5Cr0.1Si oxidized at 950 °C in Ar plus 5 vol.% H_2 with dew points of -10 °C (a) and 10 °C (b) for 1,4,16 hours are shown in Figure 4.12. The depth of internal oxidation zone of Fe-1.9Mn-1.0Cr-0.1Si oxidized at 950 °C in Ar plus 5 vol.% H_2 with dew points of -10 °C (a) and 10 °C (b) for 1,4,16 hours are shown in Figure 4.13. The data are least square linear fitted. The growth of the internal oxidation zone depth follows parabolic growth rate law as predicted. This indicates that the internal oxidation of Fe-Mn-Cr alloys is a diffusion controlled process and the diffusivities of reacting species (dissolved oxygen, manganese and chromium) as well as the boundary conditions are constant during the oxidation process.

The measured parabolic rate constants are listed in Table 4.2. The parabolic rate constants increase with dew point.

Table 4.2 Measured parabolic rate constant (see Eq.(2.3))

	DP-10 °C	**DP10 °C**
Fe-1.8Mn-1.5Cr-0.1Si	k_p =2.2 μm/h$^{1/2}$	k_p =4.7 μm/h$^{1/2}$
Fe-1.9-Mn-1.0Cr-0.1Si	k_p =2.5 μm/h$^{1/2}$	k_p =4.9 μm/h$^{1/2}$

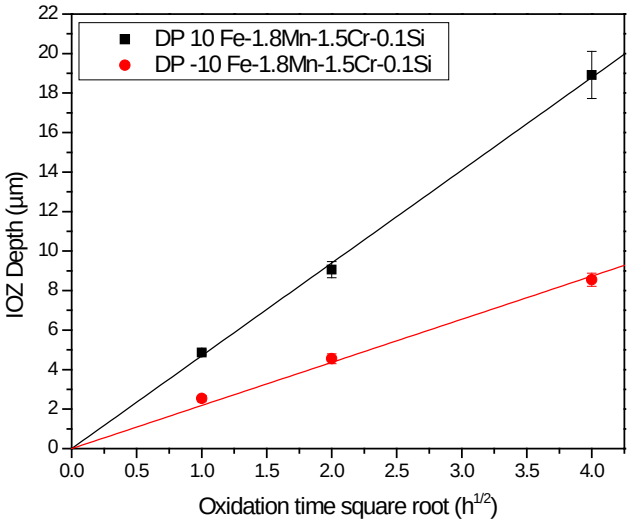

Figure 4.12 Parabolic growth of internal oxidation zone of Fe-1.8Mn-1.5Cr-0.1Si steel alloys oxidized at 950 °C in Ar plus 5 vol.% H_2 gas mixtures with dew points of -10 °C and 10 °C.

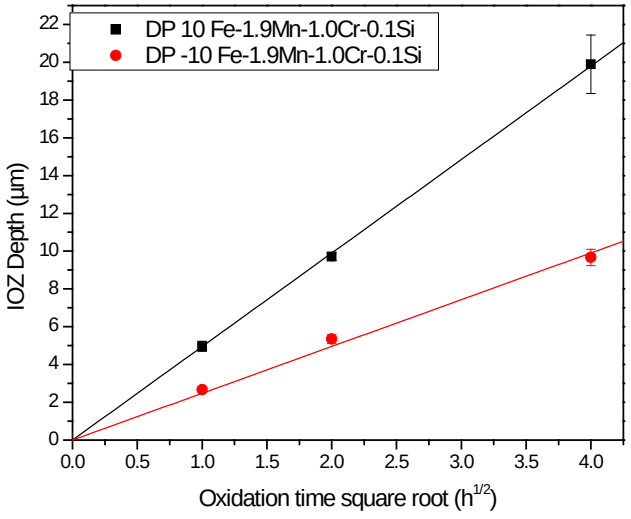

Figure 4.13 Parabolic growth of internal oxidation zone of Fe-1.9Mn-1.0Cr-0.1Si alloys oxidized at 950 °C in Ar plus 5 vol.% H_2 gas mixtures with dew points of -10 °C and 10 °C.

4.6.2 Effect of Cr addition on parabolic growth rate of IOZ

The parabolic rate constants decrease with Cr concentration. A comparison of the internal oxidation kinetics of Mn and Cr in Fe-Mn-Cr alloys with different Cr concentration oxidized at 950 °C in Ar plus 5 vol.% H_2 with dew points of -10 °C and

10 °C are shown in Figure 4.14. The parabolic rate constant is decreased with the addition of Cr. Adding Cr will lower the kinetics of internal oxidation.

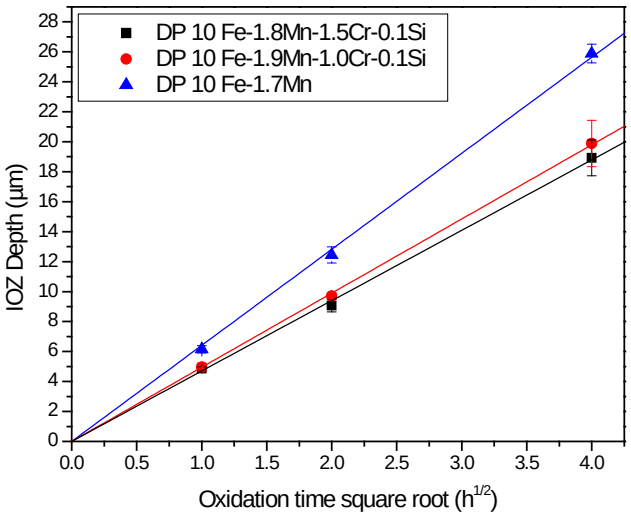

(a)

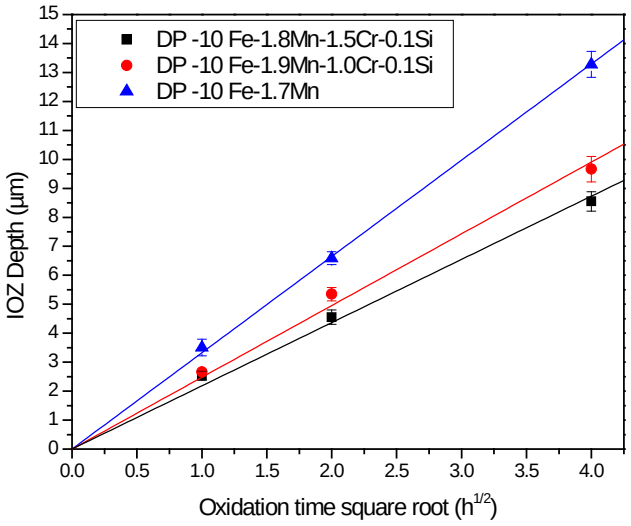

(b)

Figure 4.14 Parabolic growth of internal oxidation zone in Fe-Mn and Fe-Mn-Cr steel alloys oxidized at 950 °C in Ar plus 5 vol.% H_2 gas mixtures with dew points of -10 °C (a) and 10 °C (b).

4.6.3 Calculation of parabolic rate constant with a modified Wagner's internal oxidation theory for ternary alloy

In section 2.2, with a modified Wagner's internal oxidation theory for ternary alloy, it is obtained a general solution for γ according to Eq. (2.22). This γ solution can be further used to calculate the parabolic rate constant. If the permeability of oxygen ($D_{\mathrm{O}}N_{\mathrm{O}}$) is much larger than the permeability of alloying element B ($D_{\mathrm{B}}N_{\mathrm{B}}$) and C ($D_{\mathrm{C}}N_{\mathrm{C}}$), then parabolic rate constant can be simplified calculated with Eq. (2.26). If the permeability of oxygen ($D_{\mathrm{O}}N_{\mathrm{O}}$) is much smaller than the permeability of alloying element B ($D_{\mathrm{B}}N_{\mathrm{B}}$) and C ($D_{\mathrm{C}}N_{\mathrm{C}}$), then parabolic rate constant can be simplified calculated with Eq. (2.29).

The diffusion coefficient of oxygen in austenite steel at 950 °C here used is 3.53×10^{-7} cm^2/s. [29]. The surface mole fraction of dissolved oxygen at 950 °C in Ar plus 5 vol.% H_2 with a dew point of -10 °C is 7.541×10^{-7} and the permeability of oxygen is thus 7.541×10^{-7} mole fraction and the permeability of oxygen is 0.27×10^{-12} cm^2/s. The surface oxygen mole fraction at 950 °C in Ar plus 5 vol.% H_2 with a dew point of 10 °C is 3.57×10^{-6} and the permeability of oxygen is 1.26×10^{-12} cm^2/s.

For Fe-1.8Mn-1.5Cr-0.1Si alloy, the bulk concentration of Mn is 1.8×10^{-2} mole fraction and the bulk concentration of Cr is 1.5×10^{-2} mole fraction. For Fe-1.9Mn-1.0Cr-0.1Si alloy, the bulk concentration of Mn is 1.9×10^{-2} mole fraction and the bulk concentration of Cr is 1.0×10^{-2} mole fraction. The diffusion coefficient of Mn in γ-Fe at 950 °C here used is 4.14×10^{-12} cm^2/s [14]. The diffusion coefficient of Cr in γ-Fe here used is 1.34×10^{-12} cm^2/s [30]. Values of permeability of manganese for 1.8 and 1.9 at. % Mn concentration are 7.45×10^{-14} cm^2/s and 7.87×10^{-14} cm^2/s, respectively. Values of permeability of chromium for 1.5 and 1.0 at. % Cr concentration are 2.01×10^{-14} cm^2/s and 1.34×10^{-14} cm^2/s, respectively. Since the

permeability of oxygen is higher than manganese and chromium, the parabolic rate constant could be calculated according to Eq. (2.26). A comparison of experimental and calculated parabolic growth rate constants are listed in Table 4.3.

As can be seen in Table 4.3, the measured and calculated parabolic rate constant is in good agreement.This indicated that kinetics of internal oxidation of Fe-Mn-Cr alloys can be described by a modified Wagner theory.

Table 4.3 Comparison of experimental and calculated parabolic growth rate constants (see Eq.(2.3))

DP-10	**k_p (Experimental) (μm/h$^{1/2}$)**	**k_p(Calculated) (μm/h$^{1/2}$)**
Fe1.8Mn1.5Cr-0.1Si	2.2	2.2
Fe1.9Mn1.0Cr-0.1Si	2.5	2.4
Fe1.7Mn	3.3	3.4
DP 10	**k_p (Experimental) (μm/h$^{1/2}$)**	**k_p(Calculated) (μm/h$^{1/2}$)**
Fe1.8Mn1.5Cr-0.1Si	4.7	4.7
Fe1.9Mn1.0Cr-0.1Si	4.9	5.2
Fe1.7Mn	6.4	7.3

4.7 Depth profiles in IOZ of Fe-Mn-Cr alloys annealed at different dew points

4.7.1 Depth profiles in IOZ of Fe-Mn-Cr alloys annealed at dew point 10 °C

The depth profiles of the total concentration of Mn, Cr for Fe-1.8Mn-1.5Cr-0.1Si alloys oxidized at 950 °C in Ar plus 5 vol.% H_2 with a dew point of 10 °C for 16 hours are shown in Figure 4.15. The Experimental results are in reasonable agreement with simulation results.

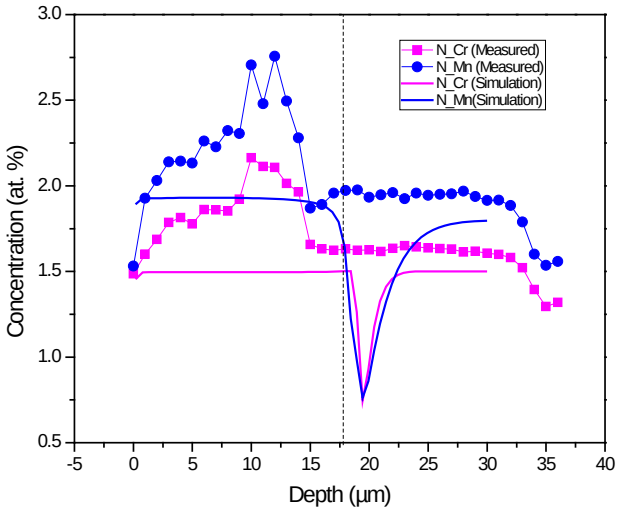

Figure 4.15 The depth profiles of the total concentration of Mn, Cr (oxides and solid solute) for Fe-1.8Mn-1.5Cr-0.1Si alloys oxidized at 950 °C in Ar plus 5 vol.% H_2 gas mixture with a dew point of 10 °C for 16 hours.

The depth profiles of the oxygen for Fe-1.8Mn-1.5Cr-0.1Si alloys oxidized at 950 °C in Ar plus 5 vol.% H_2 with a dew point of 10 °C for 16 hours are shown in Figure 4.16. The measured oxygen concentration (black line) within the IOZ is on average almost constant and decreases sharply to zero at the internal oxidation front. Thus, the internal oxides have typical features of a low solubility product oxide. Therefore, MnO and $MnCr_2O_4$ can be classified as oxides with low Ksp.

The evaluated oxygen concentration (blue line) presents the concentration of evaluated precipitated oxygen in IOZ based on EPMA measured Cr and Mn concentration. The oxygen is precipitated in two internal oxides MnO and $MnCr_2O_4$. N_O(Evaluated) is defined in Equation (4.1).

$$N\_O(Evaluated) = N\_Mn(Measured) + 3/2\, N\_Cr(Measured) \qquad (4.1)$$

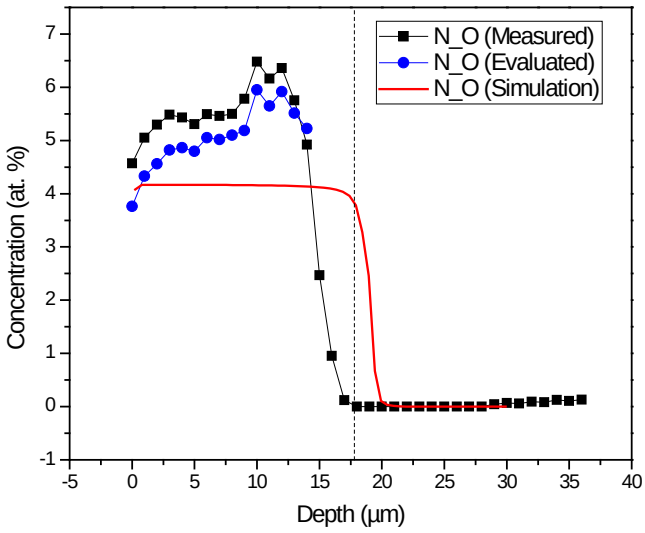

Figure 4.16 The depth profiles of oxygen for Fe-1.8Mn-1.5Cr-0.1Si alloys oxidized at 950 °C in Ar plus 5 vol.% H2 with a dew point of 10 °C for 16 hours.

Evaluated oxygen concentration is lower than EPMA measured value. There are three possible reasons for excess oxygen in EPMA measured Oxygen concentration data:

1. The measured Oxygen concentration in EPMA experiments is not accurate
2. The solute O in matrix caused the higher oxygen concentration in EPMA Experiments than evaluated oxygen concentration
3. Fe dissolution in oxides caused the excess oxygen consumption

Since the solubility of oxygen in this tested sample is very low, the most possible reason could be the iron dissolution in oxides caused the excess oxygen consumption.

The mole fraction of two internal oxides MnO and $MnCr_2O_4$ as a function of depth is shown in Figure 4.17. The mole fraction of MnO is higher than $MnCr_2O_4$ in IOZ and MnO concentration in IOZ decreases with depth. The ratio of Mole fraction of MnO and MnCr2O4 measured is approximate 1.4 (see figure 4.18). $N\_MnCr_2O_4$ (Evaluated) and N_MnO (Evaluated) are estimated with Eqs. (4.2) (4.3).

$$N\_MnCr_2O_4(\text{Evaluated}) = N\_Cr(\text{Measured}) / 2 \quad (4.2)$$

$$N\_MnO(\text{Evaluated}) = N\_Mn(\text{Measured}) - N\_MnCr_2O_4(\text{Measured}) \quad (4.3)$$

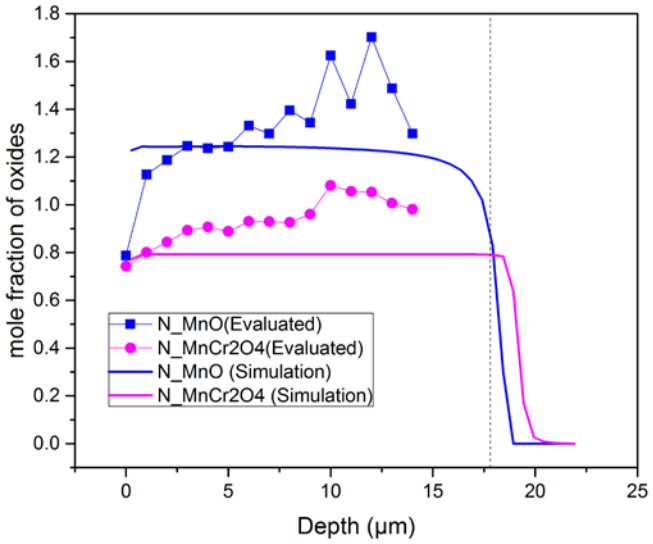

Figure 4.17 The depth profiles of the mole fraction of two internal oxides MnO and $MnC_{r2}O_4$ for Fe-1.8Mn-1.5Cr-0.1Si alloys oxidized at 950 °C in Ar plus 5 vol.% H_2 gas mixture with a dew point of 10 °C for 16 hours.

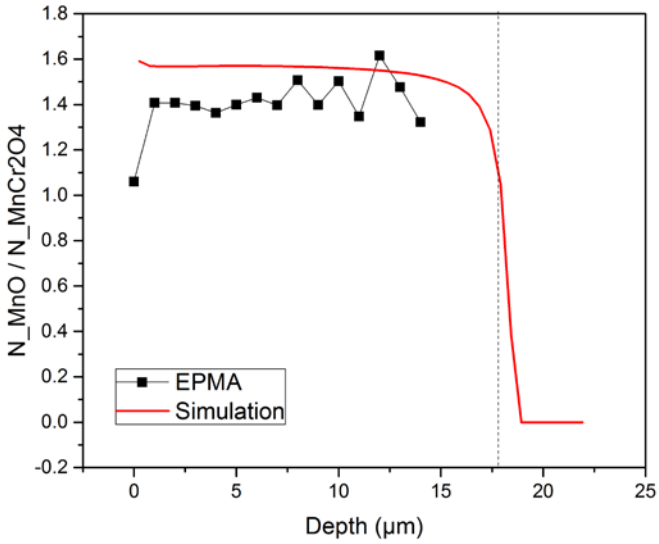

Figure 4.18 The depth profiles of the molar ratio of two internal oxides MnO and $MnC_{r2}O_4$ for Fe-1.8Mn-1.5Cr-0.1Si alloys oxidized at 950 °C in Ar plus 5 vol.% H_2 with a dew point of 10 °C for 16 hours.

Concentration depth profile of volume fraction of internal oxides obtained from EPMA, binary image analysis and simulations are compared in Figure 4.19 for the Fe-1.8Mn-1.5Cr-0.1Si alloy oxidized at 950 °C in Ar plus 5 vol.% H_2 with a dew point of 10 °C for 16 hours. The result of image analysis is in agreement with EPMA experimental results. The binary image analysis is done in the same area as EPMA measurement (see Figure 4.20). The volume fraction of internal oxides evaluated from EPMA experiments is according to Eq. (4.4), (4.5). The molar volume of iron, MnO, and $MnCr_2O_4$ are 7.10×10^{12}, 1.31×10^{13} and 4.50×10^{13} μm^3/mol, respectively.

$$\text{Internal Oxides Volume fraction} = \frac{\text{Internal Oxides Volume}}{\text{Internal Oxides Volume} + \text{N\_Fe(Measured)} * \text{Vm(Fe)}} \quad (4.4)$$

$$\text{Internal Oxides Volume} = \frac{(\text{Ratio}_{\text{MnO/MnCr}_2\text{O}_4} * \text{Vm(MnO)} + \text{Vm}(\text{MnCr}_2\text{O}_4)) * \text{N\_O}}{4 + \text{Ratio}_{\text{MnO/MnCr}_2\text{O}_4}} \quad (4.5)$$

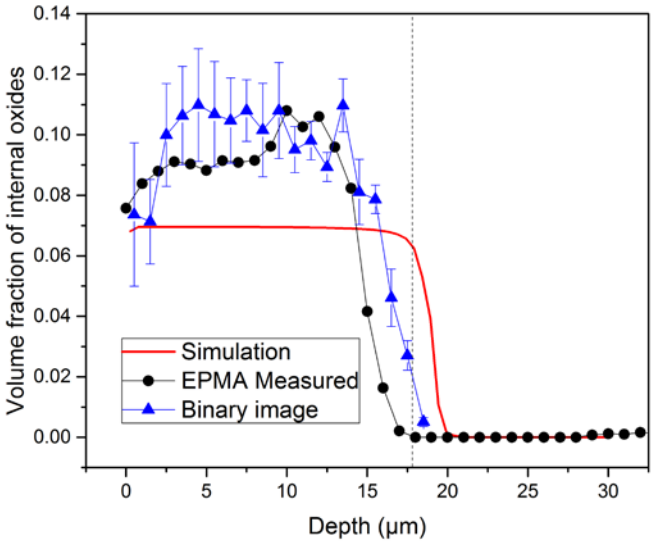

Figure 4.19 Concentration depth profile of volume fraction of internal oxides obtained from, EPMA, binary image analysis and simulations for the Fe-1.8Mn-1.5Cr-0.1Si alloy oxidized at 950 °C in Ar plus 5 vol.% H_2 with a dew point of 10 °C for 16 hours.

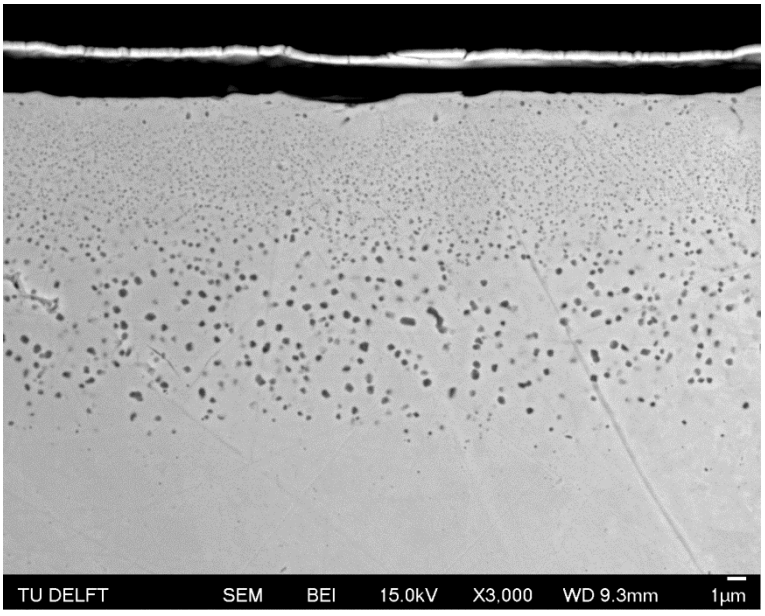

Figure 4.20 Backscattered electron images of the cross-section for the Fe-1.8Mn-1.5Cr-0.1Si alloy oxidized at 950 °C in Ar plus 5 vol.% H_2 with a dew point of 10 °C for 16 hours.

As shown in Figure 4.20, the size and number density of internal oxide precipitates are changed with depth. In depth range around 1 to 6 micron, the size of internal oxides precipitates is small and the number density is large. In depth range around 6 to 17 micron, the size of internal oxide precipitates is large and the number density of internal oxide precipitates is small. The volume fraction of internal oxides in these two areas are almost the same.

As it is discussed above, the most probable reason for the excess oxygen in EPMA measured oxygen concentration data is the iron dissolution in oxides caused the excess oxygen consumption. To obtain the concentration of excess oxygen, the mole fraction of Fe, Mn, Cr, O in monoxide and spinel oxide are calculated in Factsage. Here it is used N_O(excess) to present the excess oxygen concentration in both monoxide and spinel. N_O(excess) is defined as:

$$N\_O(excess) = N\_O(excess)_{spinel} + N\_O(excess)_{monoxide} \quad (4.6)$$

N_O(Corrected) presents the concentration of evaluated precipitated oxygen in IOZ considering iron dissolution. N_O(Corrected) is defined as:

$$N\_O(Corrected) = N\_O(Evaluated) + N\_O(excess) \quad (4.7)$$

To obtain the N_O(Corrected) as a function of depth, knowledge of the $\log(p_{O2})$ and mole fraction of oxygen as a function of depth for the tested sample of Fe-1.8Mn-1.5Cr-0.1Si alloy oxidized at 950 °C in Ar plus 5 vol.% H_2 with a dew point of 10 °C for 16 hours is essential (see Figure 4.21). The measured depth of IOZ where EPMA measurement was performed is around 17.5 micron.

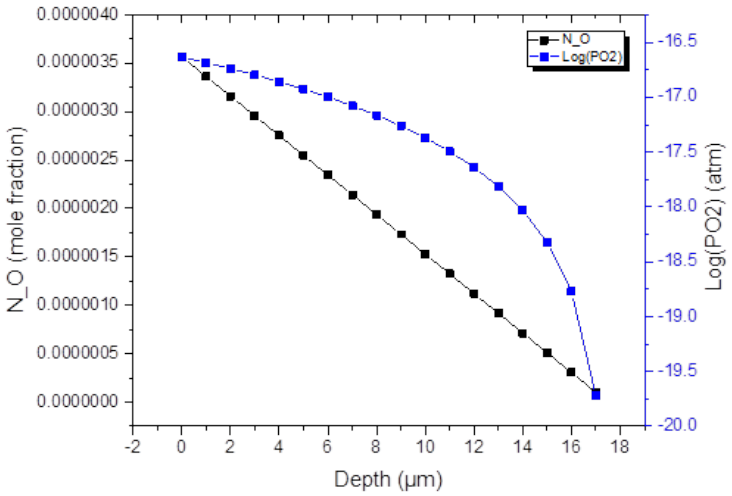

Figure 4.21 Log(pO_2) and mole fraction of oxygen as a function of depth for the Fe-1.8Mn-1.5Cr-0.1Si alloy oxidized at 950 °C in Ar plus 5 vol.% H_2 gas mixture with a dew point of 10 °C for 16 hours.

Here it is assumed that if the iron dissolved into the spinel and monoxide, then the chemical formula is presented as $(Mn,Cr)_{3-x}Fe_xO_4$ and $(Mn_{1-y}Fe_y)O$. x presents the iron content of iron dissolved in spinel and y presents the iron content of iron dissolved in monoxide. By setting up the equilibrium condition and oxygen activity in form of log(pO_2) obtained from Figure 4.20 in Factsage, it is able to calculate the x and y value as below:

$$x \ in \ (Mn,Cr)_{3-x}Fe_xO_4 = \frac{Fe_{(spinel)}}{Fe_{(spinel)} + Mn_{(spinel)} + Cr_{(spinel)}} * 3 \qquad (4.8)$$

$$y \ in \ (Mn_{1-y},Fe_y)O = \frac{Fe_{(monoxide)}}{Fe_{(monoxide)} + Mn_{(monoxide)}} * \frac{1}{1} \qquad (4.9)$$

$Fe_{(spinel)}$, $Mn_{(spinel)}$ and $Cr_{(spinel)}$ are the mole fraction of Fe, Mn and Cr among cations in spinel oxide calculated by Factsage. $Fe_{(monoxide)}$, and $Mn_{(monoxide)}$ are the mole fraction of Fe, and Mn among cations in monoxide calculated by Factsage. The calculations of x and y are independent of experimental results.

There are three approaches to obtain the N_O(excess) with different assumptions as listed in Appendix E. The results of three approaches are in agreement with each other. Here the results of approach 3 are selected.

Figure 4.22 shows the comparison of oxygen concentration depth profiles of EPMA measured (black line), evaluated value (blue line), simulation results (red line) and corrected oxygen data calculated by approach 3 (green line). The green line is perfectly matched with the black line. This indicates that the depth profile of evaluated oxygen concentration which only based on Mn and Cr after corrected with the excess oxygen consumed by iron dissolution will in a good agreement with the EPMA measured results. Therefore, it is proved that the iron dissolved in oxides cause the excess oxygen consumption for Fe-1.8Mn-1.5Cr-0.1Si alloy oxidized at 950 °C in Ar plus 5 vol.% H_2 with a dew point of 10 °C for 16 hours.

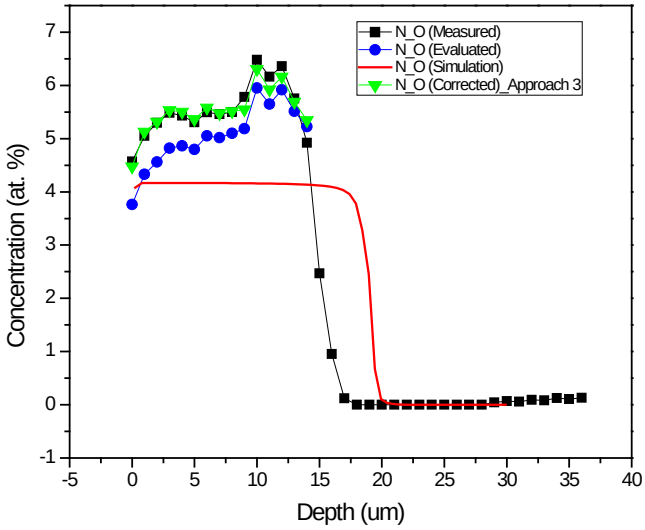

Figure 4.22 Comparison of oxygen concentration depth profiles of EPMA measured (black line), evaluated value (blue line), simulation results (red line) and corrected oxygen data calculated by approach 3 (green line).

Figure 4.23 shows the comparison of the two ratios, the black one presents the ratio of measured oxygen concentration to evaluated oxygen concentration and the red one presents the ratio of corrected oxygen concentration to evaluated oxygen concentration. There are two approaches to obtain the ratio of measured oxygen concentration to evaluated oxygen concentration (see Appendix F) and here it is used the results of approach 2.

It is worth noticing that N_O(Evaluated) is obtained only based on experimental data while N_O(corrected) is obtained from Factsage calculation and Experimental data. Therefore, the agreement of two ratios as shown in Figure 4.23 also proved the iron could dissolve in oxides cause the excess oxygen consumption for Fe-1.8Mn-1.5Cr-0.1Si alloy oxidized at 950 °C in Ar plus 5 vol.% H_2 with a dew point of 10 °C for 16 hours as discussed above.

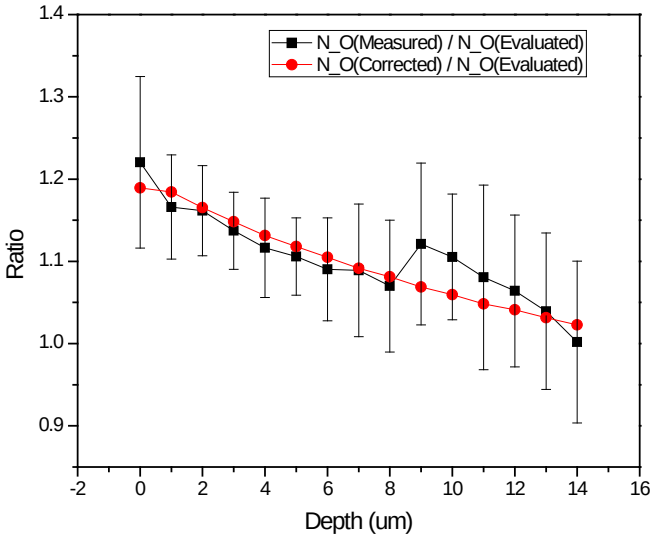

Figure 4.23 Comparison of the two ratios, the black one presents the ratio of N_O(Measured) to N_O(Evaluated) and the red one presents the ratio of N_O(Corrected) to N_O(Evaluated).

4.7.2 Depth profile in IOZ of Fe-Mn-Cr alloys at dew point -10 °C

The depth profiles of the total concentration of Mn, Cr for Fe-1.8Mn-1.5Cr-0.1Si alloys oxidized at 950 °C in Ar plus 5 vol.% H_2 with a dew point of -10 °C for 16 hours are shown in Figure 4.24. The Experimental results are in reasonable agreement with simulation results.

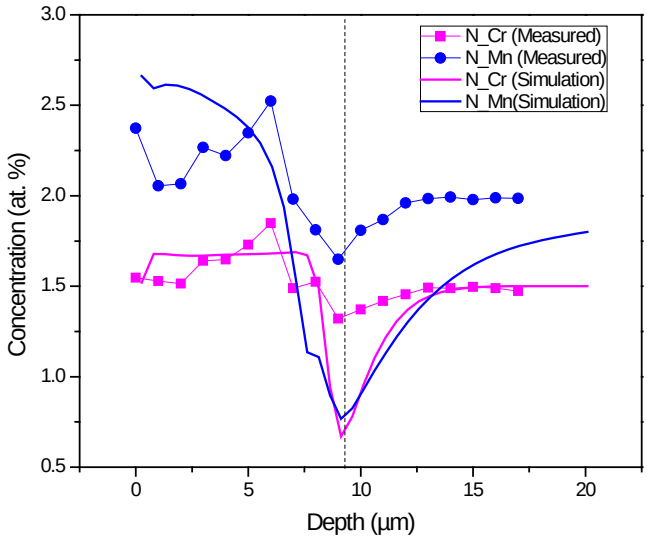

Figure 4.24 The depth profiles of the total concentration of Mn, Cr (oxides and solid solute) for Fe-1.8Mn-1.5Cr-0.1Si alloys oxidized at 950 °C in Ar plus 5 vol.% H_2 gas mixture with a dew point of -10 °C for 16 hours.

The depth profiles of the oxygen for Fe-1.8Mn-1.5Cr-0.1Si alloys oxidized at 950 °C in Ar plus 5 vol.% H_2 with a dew point of -10 °C for 16 hours are shown in Figure 4.25. The measured oxygen concentration (black line) within the IOZ is on average almost constant and decreases sharply to zero at the internal oxidation front. Thus, the internal oxides have typical features of a low solubility product oxide. Therefore, MnO and $MnCr_2O_4$ can be classified as oxides with low Ksp. The evaluated oxygen concentration (blue line) presents the concentration of evaluated precipitated oxygen in IOZ based on EPMA measured Cr and Mn concentration. The oxygen is precipitated in two internal oxides MnO and $MnCr_2O_4$. N_O(Evaluated) is defined in Equation (4.1).

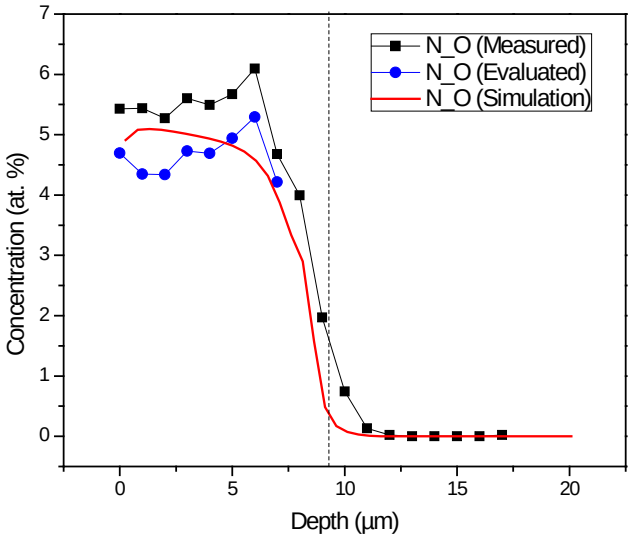

Figure 4.25 The depth profiles of oxygen for Fe-1.8Mn-1.5Cr-0.1Si alloys oxidized at 950 °C in Ar plus 5 vol.% H2 with a dew point of -10 °C for 16 hours.

Evaluated oxygen concentration is lower than EPMA measured value. According to the Factsage calculation, the iron content of iron dissolved in spinel x and the iron content of iron dissolved in monoxide y are very small, around 4.7702×10^{-2} and 4.54×10^{-2}, respectively. Therefore, the excess oxygen concentration consumed by iron is also very small. Iron dissolution in oxides is not a main reason for the difference of evaluated oxygen concentration and measured oxygen concentration. The measured oxygen concentration in EPMA experiments maybe not accurate.

The mole fraction of two internal oxides MnO and $MnCr_2O_4$ as a function of depth is shown in Figure 4.26. The mole fraction of MnO is higher than $MnCr_2O_4$ in IOZ. MnO concentration in IOZ decreases with depth according to simulation results. The ratio of Mole fraction of MnO and $MnCr_2O_4$ measured is approximate 1.8 (see figure 4.27). N_$MnCr_2O_4$ (Evaluated) and N_MnO (Evaluated) are defined in Equation (4.2) (4.3).

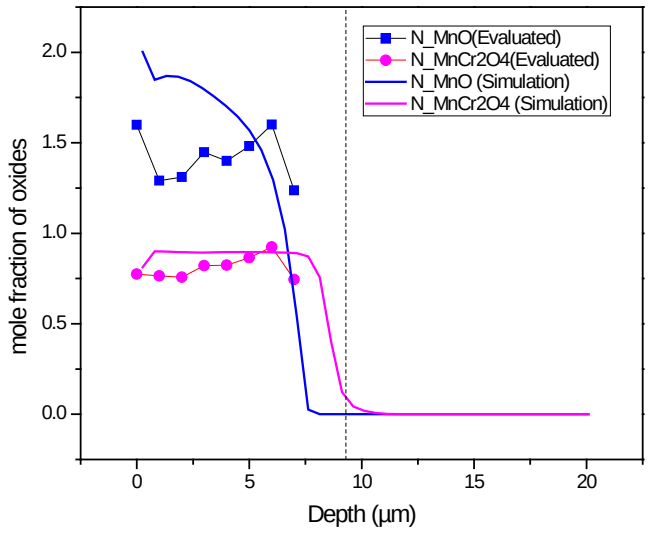

Figure 4.26 The depth profiles of the mole fraction of MnO and $MnC_{r2}O_4$ for Fe-1.8Mn-1.5Cr-0.1Si alloys oxidized at 950 °C in Ar plus 5 vol.% H_2 with a dew point of -10 °C for 16 hours.

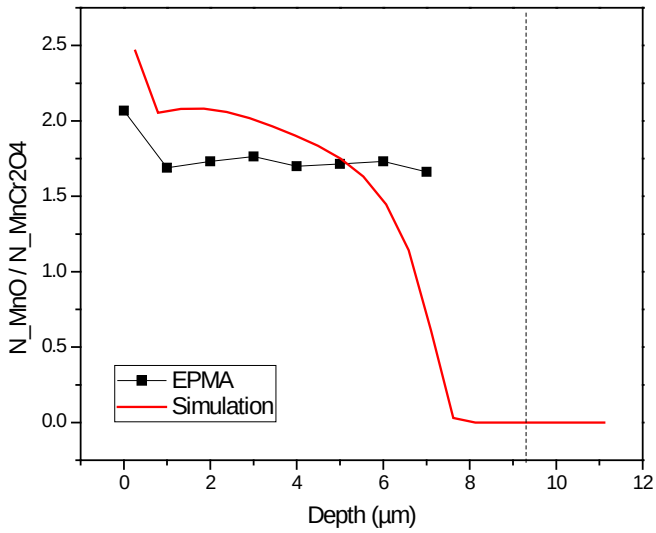

Figure 4.27 The depth profiles of the molar ratio of MnO and $MnC_{r2}O_4$ for Fe-1.8Mn-1.5Cr-0.1Si alloys oxidized at 950 °C in Ar plus 5 vol.% H_2 with a dew point of -10 °C for 16 hours.

Concentration depth profile of volume fraction of internal oxides obtained from, EPMA, binary image analysis and simulations are compared in Figure 4.28 for the Fe-1.8Mn-1.5Cr-0.1Si alloy oxidized at 950 °C in Ar plus 5 vol.% H_2 with a dew

point of -10 °C for 16 hours. The binary image analysis is done in the same area as EPMA grid measurement. The volume fraction of internal oxides evaluated from EPMA experiments is according to Eq. (4.4), (4.5). Volume fraction of Internal oxides in fine oxides layer and coarse oxides layer is almost the same. The result of image analysis is in agreement with EPMA experimental results.

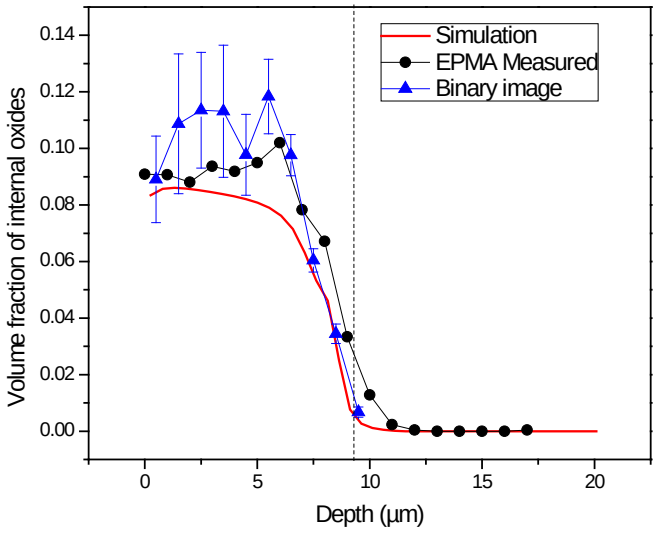

Figure 4.28 Concentration depth profile of volume fraction of internal oxides obtained from, EPMA, binary image analysis and simulations for the Fe-1.8Mn-1.5Cr-0.1Si alloy oxidized at 950 °C in Ar plus 5 vol.% H_2 with a dew point of -10 °C for 16 hours.

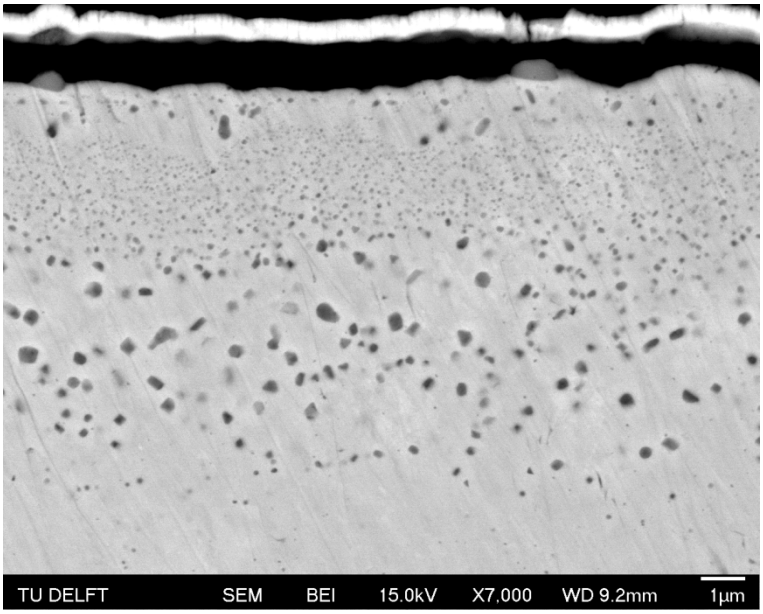

Figure 4.29 Backscattered electron images of the cross-section for the Fe-1.8Mn-1.5Cr-0.1Si alloy oxidized at 950 °C in Ar plus 5 vol.% H_2 with a dew point of -10 °C for 16 hours.

As shown in Figure 4.29, the size and number density of internal oxide precipitates are changed with depth. In depth range around 1 to 3 micron, the size of internal oxides precipitates is small and the number density is large. In depth range around 3 to 8 micron, the size of internal oxide precipitates is large and the number density of internal oxide precipitates is small. The volume fraction of internal oxides in these two areas are almost the same.

4.8 Effect of annealing atmosphere on formation of external oxides

4.8.1 Direct reduction of external oxides

Figure 4.30 shows the surfaces of samples Fe-1.7Mn-1.4Cr (a), Fe-1.8Mn-1.5Cr0.1Si (b) and Fe-1.8Mn-1.0Cr-0.5Si (c) oxidized at 950 °C in Ar plus 5 vol.% H_2 with a dew point of -30 °C for 1h hour then reduced at 950 °C in Ar plus 5 vol.% H_2 (dry) for 1 hour. The external oxides formed cannot be reduced in dry H_2. Coverage of

external oxides by image analysis for Fe-1.7Mn-1.4Cr, Fe-1.8Mn-1.5Cr0.1Si and Fe-1.8Mn-1.0Cr-0.5Si samples are 21-28%, 33-43% and 41-47%.

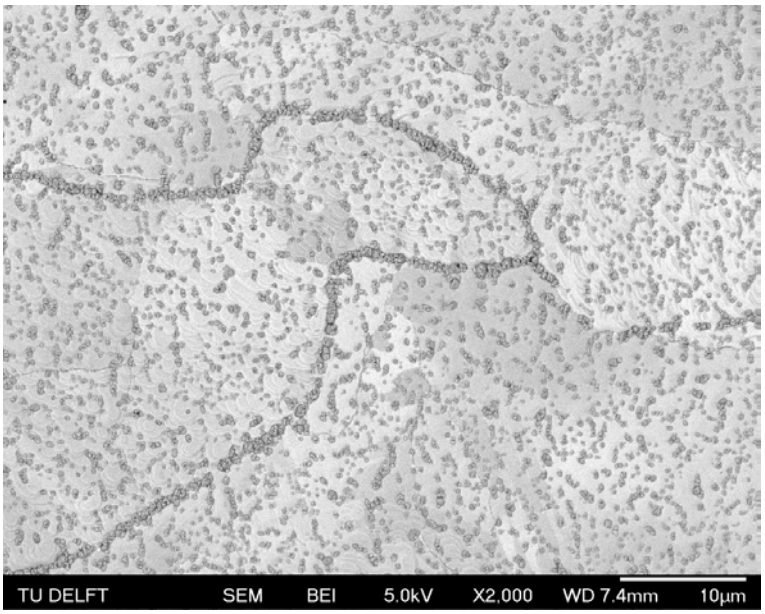

(a)

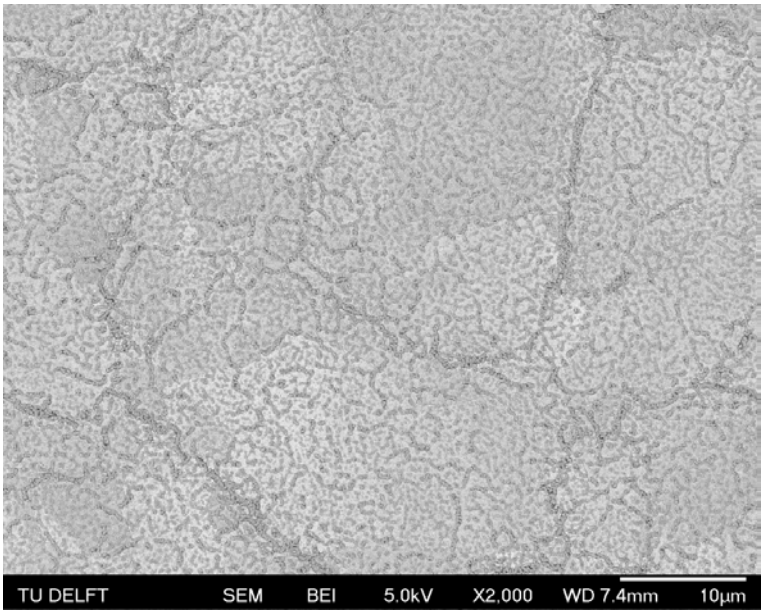

(b)

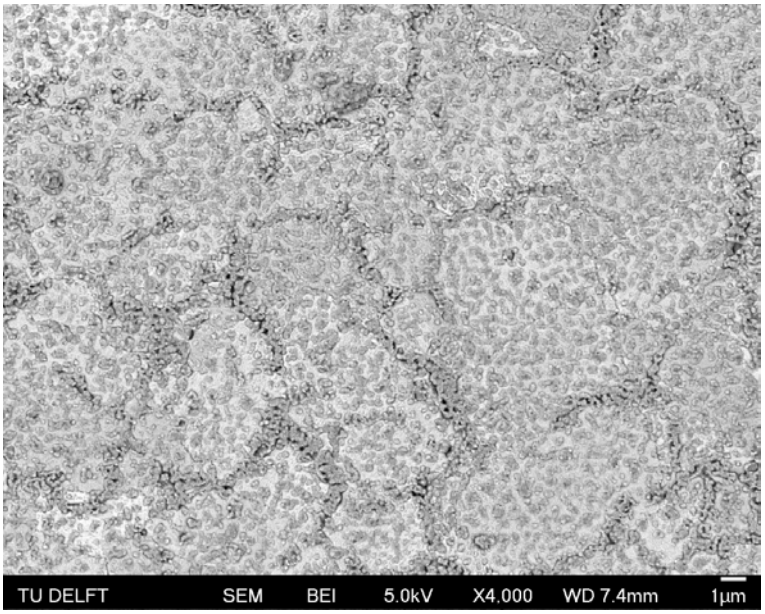

(c)

Figure 4.30 Surfaces of samples Fe-1.7Mn-1.4Cr (a), Fe-1.8Mn-1.5Cr0.1Si (b) and Fe-1.8Mn-1.0Cr-0.5Si (c) oxidized at 950 °C in Ar plus 5 vol.% H_2 with a dew point of -30 °C for 1h hour then reduced at 950 °C in Ar plus 5 vol.% H_2 (dry) for 1 hour.

4.8.2 Wüstite (FeO) formation and reduction

Figure 4.31 shows the surfaces of four samples (Fe-1.7Mn-1.4Cr, Fe-1.8Mn-1.5Cr-0.1Si, Fe-1.8Mn-1.0Cr-0.5Si and Fe-1.8Mn-2.0Si) oxidized in 50 vol.% Ar + 33 vol.% CO_2 + 17 vol.% CO gas mixture for 4h and then reduced at 950 °C in Ar+5vol.% H_2 gas mixture for 2h. The formation of wüstite is expected after annealing in Ar/ CO_2/CO gas mixtures. Then after reducing in dry Ar/ H_2 gas mixtures, wüstite is expected to be reduced to pure iron. EDS suggest for all the four samples, the light area is indeed pure iron.

For sample Fe-1.7Mn-1.4Cr, there are no external oxides observed after reduction. For the other three samples, there are still small external oxides observed after reduction. EDS suggest for these oxides contain elements Mn,Cr,Si,Al,Fe,O (see Appendix C).

It is noted that the Si contents in these four samples are different. There is no Si existed in sample Fe-1.7Mn-1.4Cr and the external oxides observed after reduction is zero. As the Si content increased from 0.1 mol% to 2.0 mol%, the coverage of external oxide particles on the reduced surfaces increased. In addition, Si promoted the formation of holes on the Fe layer formed after FeO reduction.

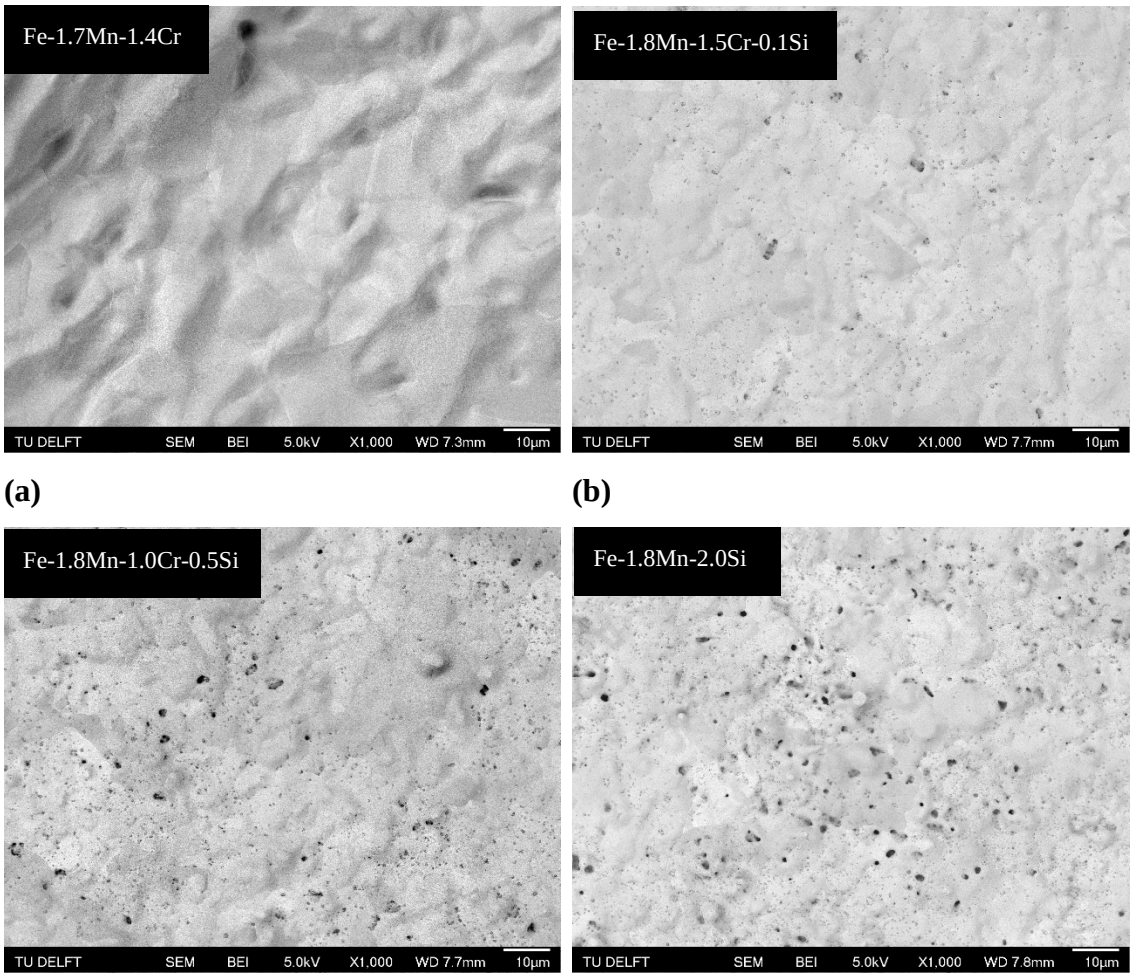

Figure 4.31 Surfaces of four samples (Fe-1.7Mn-1.4Cr, Fe-1.8Mn-1.5Cr-0.1Si, Fe-1.8Mn-1.0Cr-0.5Si and Fe-1.8Mn-2.0Si) oxidized in Ar + 33 vol.% CO2 + 17 vol.% CO gas mixture for 4h and then reduced at 950 °C in Ar+5vol.% H2 gas mixture for 2h.

CHAPTER 5

CONCLUSIONS

1) The internal oxides formed in the Fe-Mn-Cr steel alloys are (Mn, Fe)O and $(Cr, Mn, Fe)_3O_4$. The Cr_2O_3 is not formed, which is in agreement with prediction.
2) The dissolution of iron in these two internal oxides was observed and the excess oxygen concentration could be calculated in Factsage software. The calculated concentration of iron dissolution is in agreement with the experimental results. The iron concentration in Mn-Cr spinel increases with annealing dew point.
3) It was found that Fe-Mn-Cr steel alloys are externally oxidized when annealing at dew point of -45 °C, while internally oxidized at dew points of -10 and 10 °C.
4) The kinetics of internal oxidation of Fe-Mn-Cr alloys follow a parabolic growth rate law. The rate of growth of IOZ increases with dew point. The measured kinetics of internal oxidation of Fe-Mn-Cr alloys and the concentration depth profiles of internal oxides are in good agreement with simulation results. Adding Cr to the Fe-Mn steel alloys decreases the kinetics of internal oxidation. A modified Wagner's internal oxidation theory could be applied to predict the parabolic growth rate constant.
5) The external oxides formed during annealing of Fe-Mn-Cr steel alloys cannot be reduced by H_2. However, an oxide-free steel surface can be obtained by first forming and then reducing a Wüstite scale. External Si oxides can still be observed after Wüstite reduction when Si is added to the steel.

CHAPTER 6

RECOMMENDATIONS

The recommendations for the future work are listed below:

1. From the study of this project, kinetics of internal oxidation of Fe-Mn-Cr alloys can be described with a modified Wagner's internal oxidation theory. The general solution for kinetic parameter γ (Eq. (2.22)) is a key function to calculate the parabolic growth rate constant. The so-called mixed terms in the diffusion fluxes of the various components in the alloy are neglected. Therefore, further study can be performed to study the effect of mixed terms in the diffusion fluxes of the various components in the alloy on the calculation of parabolic rate constant.
2. The calculation of diffusion coefficient of Mn and Cr in the steel alloy from experimental data can be determined from the concentration depth profile of Mn and Cr in solid solution measured with handpicked measurement points with EPMA.
3. X-Ray photoelectron spectroscopy (XPS) measurement on external oxides formed on Fe-Mn-Cr alloys can be performed in order to study the concentration of each type of external oxide at different dew point and annealing time.
4. The composition of grain boundary oxides and inside grain oxides can be semi quantitative obtained by Auger Electron Spectroscopy (AES).

Reference

1. Keeler, S., *AHSS Application Guidelines*. 2014, World Steel Association.
2. Jin, Y.S., *Development of advanced high strength steels for automotive applications.* Metallurgia Italiana, 2011(6): p. 43-48.
3. Jha, G., et al., *Design and development of precipitate strengthened advanced high strength steel for automotive application.* Materials Science and Engineering: A, 2013. **561**: p. 394-402.
4. Marc Blumenau, M.N., *Overview on challenges and approaches to industrially hot-dip coat advanced high strength steels.* 2012.
5. Kuziak, R., R. Kawalla, and S. Waengler, *Advanced high strength steels for automotive industry.* Archives of Civil and Mechanical Engineering, 2008. **8**(2): p. 103-117.
6. Tsukatani, I., S. Hashimoto, and T. Inoue, *EFFECTS OF SILICON AND MANGANESE ADDITION ON MECHANICAL-PROPERTIES OF HIGH-STRENGTH HOT-ROLLED SHEET STEEL CONTAINING RETAINED AUSTENITE.* Isij International, 1991. **31**(9): p. 992-1000.
7. Hofmann, H., D. Mattissen, and T.W. Schaumann, *Advanced cold rolled steels for automotive applications.* Materialwissenschaft und Werkstofftechnik, 2006. **37**(9): p. 716-723.
8. Grajcar, A., R. Kuziak, and W. Zalecki, *Third generation of AHSS with increased fraction of retained austenite for the automotive industry.* Archives of Civil and Mechanical Engineering, 2012. **12**(3): p. 334-341.
9. Prabhudev, S., S. Swaminathan, and M. Rohwerder, *Effect of oxides on the reaction kinetics during hot-dip galvanizing of high strength steels.* Corrosion Science, 2011. **53**(7): p. 2413-2418.
10. Lins, V.d.F.C., et al., *Selective oxidation of dual phase steel after annealing at different dew points.* Applied Surface Science, 2011. **257**(13): p. 5871-5878.
11. E. M. Bellhouse , J.R.M., *Effect of Oxygen Partial Pressure during Annealing on the Selective Oxidation and Galvanizing of a 1.5% Al TRIP-Assisted Steel.* 2009.
12. Kim, Y., et al., *The influence of the dew point on the wettability of twinning-induced-plasticity steels by liquid Zn–0.23-wt% Al.* Corrosion Science, 2014. **85**: p. 364-371.
13. Liu, H., et al., *Challenges in hot-dip galvanizing of high strength dual phase steel: Surface selective oxidation and mechanical property degradation.* Surface and Coatings Technology, 2012. **206**(16): p. 3428-3436.
14. V.A.Lashgari, *Internal and External Oxidation of Manganese in Advanced High Strength Steels.* 2014.
15. Swaminathan, S. and M. Spiegel, *Thermodynamic and kinetic aspects on the selective surface oxidation of binary, ternary and quarternary model alloys.* Applied Surface Science, 2007. **253**(10): p. 4607-4619.
16. Swaminathan, S., M. Rohwerder, and M. Spiegel, *Temperature and dew point dependent segregation of phosphorus and sulfur in Fe–Mn–P–S model alloy.* Surface and Coatings Technology, 2011. **205**(16): p. 4089-4093.
17. Blumenau, M., et al., *Reactive wetting during hot-dip galvanizing of high manganese alloyed steel.* Surface and Coatings Technology, 2011. **205**(10): p. 3319-3327.

18. Wagner, C., *REAKTIONSTYPEN BEI DER OXYDATION VON LEGIERUNGEN.* Zeitschrift Fur Elektrochemie, 1959. **63**(7): p. 772-790.
19. Chatterjee, A., et al., *Kinetic modeling of high temperature oxidation of Ni-base alloys.* Computational Materials Science, 2011. **50**(3): p. 811-819.
20. Guan, S.W., H.C. Yi, and W.W. Smeltzer, *INTERNAL OXIDATION OF TERNARY ALLOYS .1. KINETICS IN THE ABSENCE OF AN EXTERNAL SCALE.* Oxidation of Metals, 1994. **41**(5-6): p. 377-387.
21. Niu, Y. and F. Gesmundo, *The internal oxidation of ternary alloys II: The coupled internal oxidation of the two most-reactive components under intermediate oxidant pressures.* Oxidation of Metals, 2003. **60**(5-6): p. 371-391.
22. N. Birks, G.H.M.a.F.S.P., *Introduction to the High Temperature Oxidation of Metals* 2006.
23. W. Mao, V.A.L., W. Melfo, W.G. Sloof, *Effect of Cr on the Oxidation of Advanced High Strength Steels during Annealing Prior to Galvanizing.* Galvatech 2015.
24. Swaminathan, S. and M. Spiegel, *Effect of alloy composition on the selective oxidation of ternary Fe-Si-Cr, Fe-Mn-Cr model alloys.* Surface and Interface Analysis, 2008. **40**(3-4): p. 268-272.
25. Wilson, P.R. and Z. Chen, *The effect of manganese and chromium on surface oxidation products formed during batch annealing of low carbon steel strip.* Corrosion Science, 2007. **49**(3): p. 1305-1320.
26. Huin, D., P. Flauder, and J.B. Leblond, *Numerical Simulation of Internal Oxidation of Steels during Annealing Treatments.* Oxidation of Metals, 2005. **64**(1-2): p. 131-167.
27. A. Sutka[a,*] , G. Mezinskis[a], and A. Lusis[b] , *Influence of iron non-stoichiometry on spinel zinc ferrite gas sensing properties.* Sensors and Actuators B, 2012. 171-172: p. 204-209
28. Natsuko Sakaia,*, Teruhisa Horita[a], *Structure and transport property of manganese–chromium–iron oxide as a main compound in oxide scales of alloy interconnects for SOFCs*, Solid State Ionics 176 (2005) 681–686.
29. Swisher, J.H. and E.T. Turkdogan, *Solubility, permeability, and diffusivity of oxygen in solid iron*. Transactions of the Metallurgical Society of AIME, 1967.239: p. 426-431.
30. D. Young, *High temperature oxidaiton and corrosion of metals*, 2nd ed.: Elsevier, 2016.

Appendix A. Dew point

The relationship between the partial pressure of water vapor and dew point is as follows:

$$\log_{P_{H_2O}} = \frac{9.8DP}{273.15+DP} - 2.22(DP \le 0°) \tag{A.1}$$

$$\log_{P_{H_2O}} = \frac{7.58DP}{240+DP} - 2.22(DP \ge 0°) \tag{A.2}$$

The oxygen partial pressure in the annealing atmosphere can be calculated according to the following equation:

$$\frac{1}{2}\log_{P_{O_2}} = 3.00 - \frac{13088}{T} + \log\frac{P_{H_2O}}{P_{H_2}} \tag{A.3}$$

The surface concentration of oxygen in mole fraction can be calculated by the following equations:

$$\log_{N_O^S} = \log\frac{P_{H_2O}}{P_{H_2}} - \frac{5000}{T} - 0.67(bcc-Fe) \tag{A.4}$$

$$\log_{N_O^S} = \log\frac{P_{H_2O}}{P_{H_2}} - \frac{4050}{T} - 1.52(fcc-Fe) \tag{A.5}$$

Appendix B. Annealing conditions of selective oxidation experiments

Table C.1. Annealing conditions of selective oxidation experiments with annealing time 1hour.

Steel sample	Sample preparation	Temperature (°C)	Gas composition	Dew point (°C) (Total Gas flow rate(ml/min))
Fe-1.7Mn	Mechanically grinded till #4000, polished with 1 micron pad	950	Ar + 5 vol.% H_2	-45(F3000), -30(F1500), -10(F1500), +10(F1500)
Fe-1.9Mn-1.0Cr-0.1Si	Mechanically grinded till #4000, polished with 1 micron pad	950	Ar + 5 vol.% H_2	-45(F3000), -30(F1500), -10(F1500), +10(F1500)
Fe-1.8Mn-1.5Cr-0.1Si	Mechanically grinded till #4000, polished with 1 micron pad	950	Ar + 5 vol.% H_2	-45(F3000), -30(F1500), -10(F1500), +10(F1500)
Fe-1.7Mn-1.4Cr	Mechanically grinded till #4000, polished with 1 micron pad	950	Ar + 5 vol.% H_2	-45(F3000)

Table C.2. Annealing conditions of selective oxidation experiments with annealing time 4 hours.

Steel sample	Sample preparation	Temperature (°C)	Gas composition	Dew point (°C) (Total Gas flow rate(ml/min))
Fe-1.7Mn	Mechanically grinded till #4000, polished with 1 micron pad	950	Ar + 5 vol.% H_2	-45(F3000), -30(F1500), -10(F1500), +10(F1500)
Fe-1.9Mn-1.0Cr-0.1Si	Mechanically grinded till #4000, polished with 1 micron pad	950	Ar + 5 vol.% H_2	-45(F3000), -30(F1500), -10(F1500), +10(F1500)
Fe-1.8Mn-1.5Cr-0.1Si	Mechanically grinded till #4000, polished with 1 micron pad	950	Ar + 5 vol.% H_2	-45(F3000), -30(F1500), -10(F1500), +10(F1500)
Fe-1.7Mn-1.4Cr	-	-	-	-

Table C.3. Annealing conditions of selective oxidation experiments with annealing time 16 hours.

Steel sample	Sample preparation	Temperature (°C)	Gas composition	Dew point (°C) (Total Gas flow rate (ml/min))
Fe-1.7Mn	Mechanically grinded till #4000, polished with 1 micron pad	950	Ar + 5 vol.% H_2	-45(F3000), -30(F1500), -10(F1500), +10(F1500)
Fe-1.9Mn-1.0Cr-0.1Si	Mechanically grinded till #4000, polished with 1 micron pad	950	Ar + 5 vol.% H_2	-45(F3000), -30(F1500), -10(F1500), +10(F1500)
Fe-1.8Mn-1.5Cr-0.1Si	Mechanically grinded till #4000, polished with 1 micron pad	950	Ar + 5 vol.% H_2	-45(F3000), -30(F1500), -10(F1500), +10(F1500)
Fe-1.7Mn-1.4Cr	Mechanically grinded till #4000, polished with 1 micron pad	950	Ar + 5 vol.% H_2	-45(F3000), -30(F1500),

Appendix C. Electron Dispersive Spectroscopy (EDS)

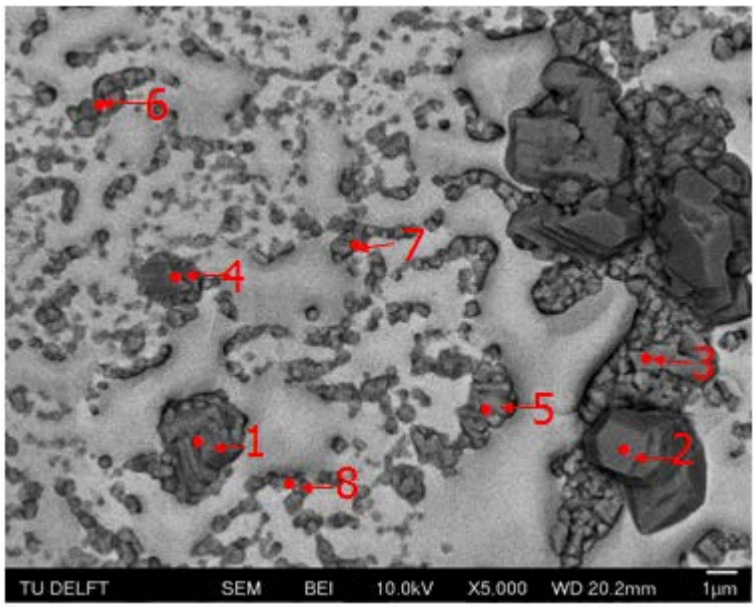

Point	Identified elements
1	Mn,Cr,O
2	Mn,O
3	Mn,O
4	Mn,O
5	Mn,Cr,O
6	Mn,O
7	Mn,Cr,Fe,O
8	Mn,Cr,Fe,O

Figure D.1 XMA analysis for the surface of Fe-1.7Mn-1.4Cr alloys annealed at 950 °C in Ar plus 5 vol.% H_2 gas mixture for 16 hours with dew points of -30 °C.

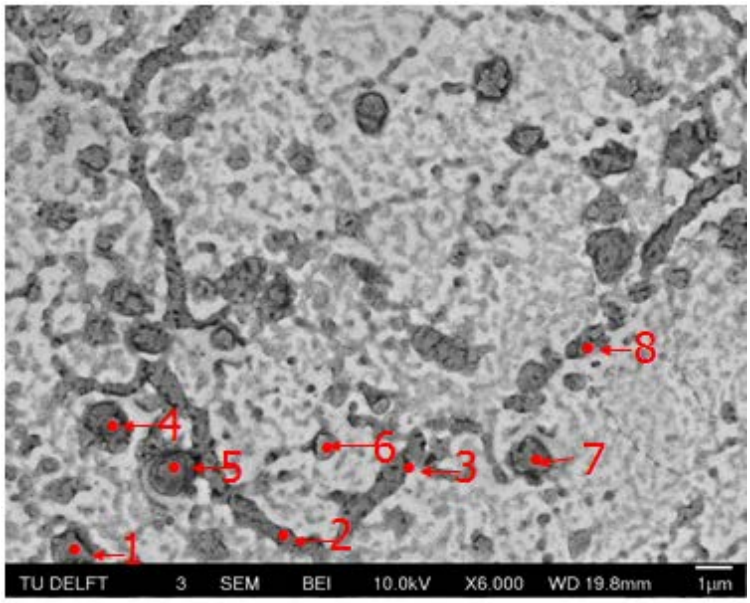

Point	Identified elements
1	Mn,O
2	Mn,Cr,Si,Fe,O
3	Mn,Cr,Si,Fe,O
4	Mn,Cr,O
5	Mn,O
6	Mn,O
7	Mn,Cr,O
8	Mn,Cr,Si,Fe,O

Figure D.2 XMA analysis for the surface of Fe-1.8Mn-1.5Cr-0.1Si alloys annealed at 950 °C in Ar plus 5 vol.% H_2 gas mixture for 1 hour with dew points of -30 °C.

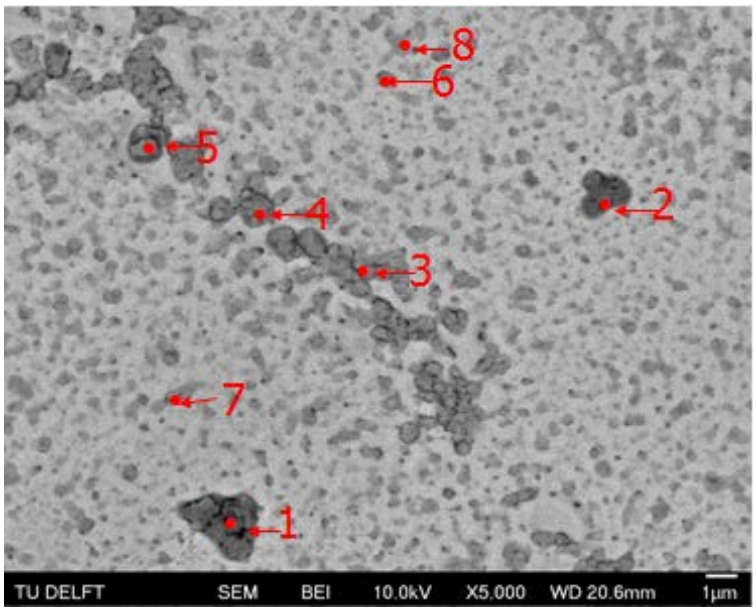

Point	Identified elements
1	Mn,Si,O
2	Mn,Si,O
3	Mn,Cr,Fe,O
4	Mn,Cr,Fe,O
5	Mn,Fe,O
6	Mn,Fe,O
7	Mn,Fe,O
8	Mn,Fe,O

Figure D.3 XMA analysis for the surface of Fe-1.8Mn-1.5Cr-0.1Si alloys annealed at 950 °C in Ar plus 5 vol.% H_2 gas mixture for 1 hour with dew points of -10 °C.

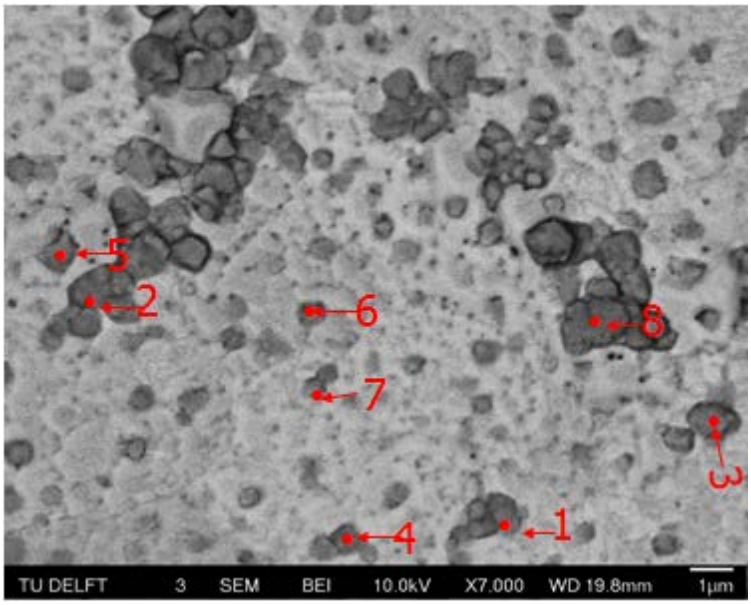

Point	Identified elements
1	Mn,Fe,O
2	Mn,Cr,Fe,O
3	Mn,Cr,Fe,O
4	Mn,Fe,O
5	Mn,Fe,O
6	Mn,Fe,O
7	Mn,Fe,O
8	Mn,Cr,Fe,O

Figure D.4 XMA analysis for the surface of Fe-1.8Mn-1.5Cr-0.1Si alloys annealed at 950 °C in Ar plus 5 vol.% H_2 gas mixture for 1 hour with dew points of 10 °C.

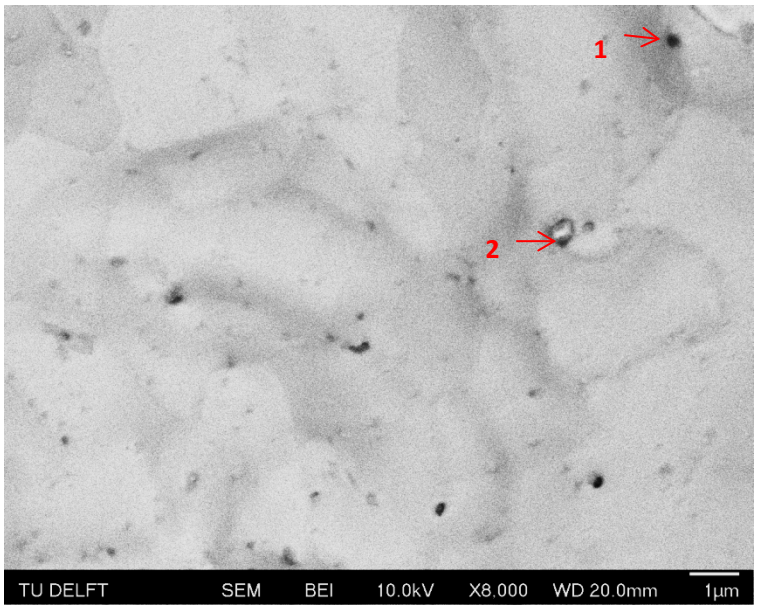

Point	Identified elements
1	Mn,Cr,Si,Al,Fe,O
2	Mn,Cr,Si,Al,Fe,O

Figure D.5 XMA analysis for the surface of Fe-1.8Mn-1.5Cr-0.1Si oxidized in Ar + 33 vol.% CO_2 + 17 vol.% CO gas mixture for 4h and then reduced at 950 °C in Ar+5vol.% H2 gas mixture for 2h.

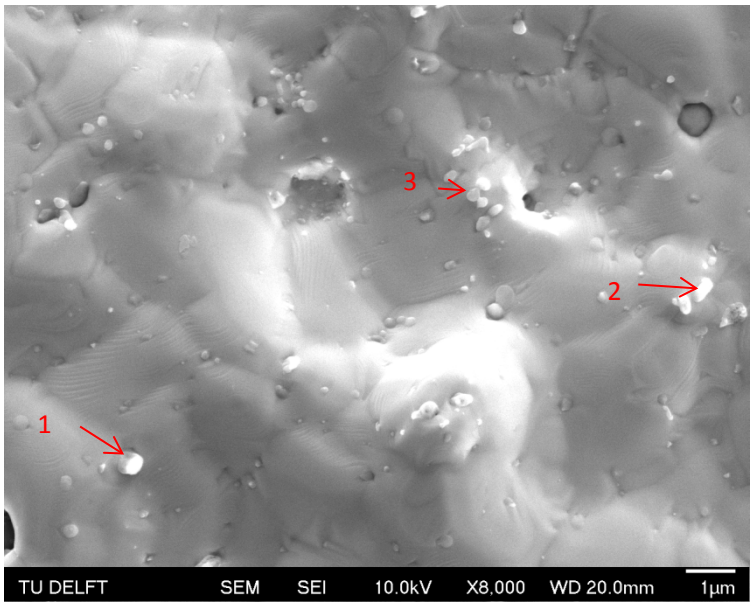

Point	Identified elements
1	Mn,Cr,Si,Al,Fe,O
2	Mn,Cr,Si,Al,Fe,O
3	Mn,Cr,Si,Al,Fe,O

Figure D.6 XMA analysis for the surface of Fe-1.8Mn-1.0Cr-0.5Si oxidized in Ar + 33 vol.% CO_2 + 17 vol.% CO gas mixture for 4h and then reduced at 950 °C in Ar+5vol.% H2 gas mixture for 2h.

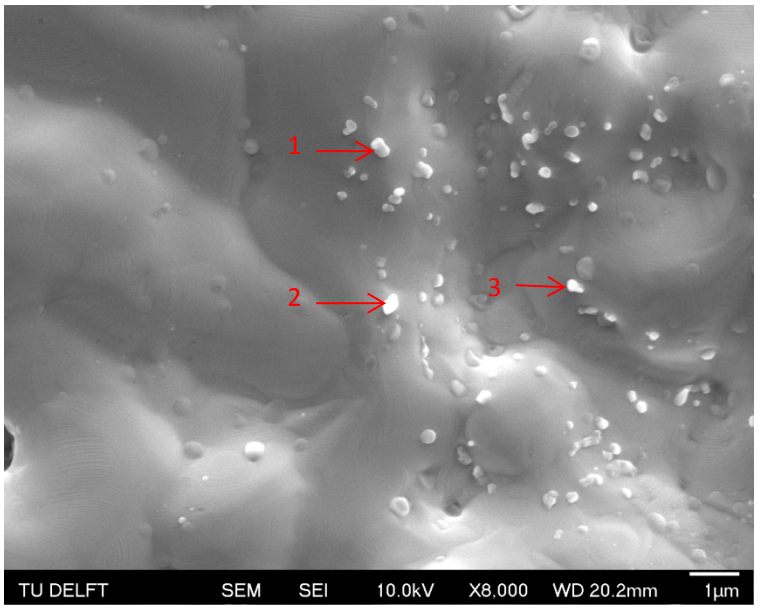

Point	Identified elements
1	Mn,Si, Fe,O
2	Mn,Si,Al,Fe,O
3	Mn,Si,Al,Fe,O

Figure D.7 XMA analysis for the surface of Fe-1.8Mn-2.0Si oxidized in Ar + 33 vol.% CO_2 + 17 vol.% CO gas mixture for 4h and then reduced at 950 °C in Ar+5vol.% H2 gas mixture for 2h.

Appendix D. PDF Card

PDF Number	Quality Mark	Chemical Formula	Rad	a
04-002-1873	Indexed	$Cr_2 Mn O_4$	CuKá1	8.43400
04-002-1874	Indexed	$Cr_2 Mn O_4$	CuKá1	8.42500
04-002-1875	Indexed	$Cr_2 Mn O_4$	CuKá1	8.42400
04-002-3802	Indexed	$Cr_2 Mn O_4$	CuKá1	8.43500
04-006-2565	Indexed	$Cr_2 Mn O_4$	CuKá1	8.43700
00-054-0876	Indexed	$Cr_2 Mn O_4$	CuKá1	8.44054
01-075-1614	Indexed	$Cr_2 Mn O_4$	CuKá1	8.43720
00-034-0140	star	$Cr_2 Fe O_4$	CuKá1	8.37900
04-016-4072	star	$Cr_2 Fe O_4$	CuKá1	8.37652
04-013-6574	Star	Fe2 Mn O4	CuKá1	8.51261
04-016-1572	Star	Fe2 Mn O4	CuKá1	8.49832

Appendix E. Calculation of Iron Dissolution in oxides

There are three approaches to obtain the N_O(excess) with different assumptions.

For the first approach, there are four assumptions:

1) Mn-Cr spinel oxide is stoichiometry oxide and written in AB_2O_4 form. Mn is fixed at A position and Cr is fixed at B position.
2) The ratio of the concentration of Cr and Mn in spinel oxide is always equaled to 2.
3) The ratio of the concentration of O and Fe in spinel oxide is always equaled to 4/3.
4) The ratio of MnO to $MnCr_2O_4$ is fixed 1.4.

The ratio of N_O(Corrected)/N_O(Evaluated) could be obtained according to Eq. (E.1)

$$\text{N\_O(Corrected)} / \text{N\_O(Evaluated)} = \frac{2*x/(3-x)+1.4/2*y/(1-y)}{(2+1.4/2)+1} \qquad \text{(E.1)}$$

x and y are obtained from Factsage calculation.

For the second approach, there are four assumptions:

1) Mn-Cr spinel oxide is stoichiometry oxide and written in AB_2O_4 form. Mn is fixed at A position and Cr is fixed at B position.
2) The ratio of the concentration of Cr and Mn in spinel oxide is always equaled to 2.
3) The ratio of the concentration of O and Fe in spinel oxide is always equaled to 4/3.

The concentration of oxygen consumed by iron in spinel oxide and monoxide could be obtained by Eq. (E.2) and Eq. (E.3), respectively.

$$N\_O(excess)_{spinel} = \frac{x}{3-x} * 2 * N\_Cr(measured) \quad (E.2)$$

$$N\_O(excess)_{monoxide} = \frac{y}{1-y}(N\_Mn(measured) - N\_Cr(measured)/2) \quad (E.3)$$

x and y are obtained from Factsage calculation.

$N\_O(excess)_{spinel}$ and $N\_O(excess)_{monoxide}$ present the concentration of oxygen consumed by iron in spinel oxide and monoxide.

The ratio of N_O(Corrected)/N_O(Evaluated) could be obtained according to Eq. (E.4)

$$\frac{N\_O(excess)_{spinel} + N\_O(excess)_{monoxide} + N\_O(Evaluated)}{N\_O(Evaluated)} \quad (E.4)$$

For the third approach, the only assumption used in the first assumption in approach one. It is still considering Mn-Cr spinel oxide as stoichiometry oxide and written in AB_2O_4 form. Mn is fixed at A position and Cr is fixed at B position.

Since the assumption is simpler than approach one, here need to induce three more parameters u, v, w to describe the calculation process. The chemical formulas for spinel and monoxide are presented as $(Mn_1, Fe_u)(Cr_{Cr_{(spinel)}/Mn_{(spinel)}}, Fe_v)O_{1+u+\frac{3}{2}(Cr_{(spinel)}/Mn_{(spinel)}+v)}$ and $(Mn_1, Fe_w)O_{(1+w)}$. Parameters u, v presents the mole fraction of iron at A position in spinel and B position, respectively. Parameter w presents the mole fraction of iron at A position in monoxide.

Since it is assumed that the Mn-Cr spinel oxide is stoichiometry oxide and written in AB_2O_4 form, the mole fraction of ions at A position is always half than that at B

position. Therefore, the relation between u and v could be presented in Equation (E.5).

$$\frac{1+u}{1*Cr_{(spinel)}/Mn_{(spinel)}+v}=\frac{1}{2} \tag{E.5}$$

Since the $Fe_{(spinel)}$, $Mn_{(spinel)}$ and $Cr_{(spinel)}$ at every certain depth could be calculated by Factsage, the relation between u and v could also be presented in Equation (E.6).

$$C=\frac{Fe_{(spinel)}}{Mn_{(spinel)}+Cr_{(spienl)}}=\frac{u+v}{1+1*Cr_{(spinel)}/Mn_{(spinel)}} \tag{E.6}$$

Thus, u and v can be obtained solving Equation (E.5) and Equation (E.6).

$$u=\frac{C+(1+C)Cr_{(spinel)}/Mn_{(spinel)}-2}{3} \tag{E.7}$$

$$v=\frac{2+2C+(2C-1)Cr_{(spinel)}/Mn_{(spinel)}}{3} \tag{E.8}$$

Parameter w can be calculated using Equation (E.9).

$$w=\frac{Fe_{(monoxide)}}{Mn_{(monoxide)}} \tag{E.9}$$

The concentration of iron dissolved in spinel oxide could be calculated using Equation (E.10) and Equation (E.11).

$$N\_Fe(u)=\frac{N\_Cr(measured)*u}{Cr_{(spinel)}/Mn_{(spinel)}} \tag{E.10}$$

$$N\_Fe(v)=\frac{N\_Cr(measured)*v}{Cr_{(spinel)}/Mn_{(spinel)}} \tag{E.11}$$

N_Fe(u) and N_Fe(v) present the concentration of iron dissolved at A position and B position, respectively.

The concentration of iron dissolved in monoxide could be calculated using Equation (E.12).

$$N\_Fe(w) = w^{*}\left[N\_Mn(measured) - \frac{N\_Cr(measured)}{\left(Cr_{(spinel)} / Mn_{(spinel)}\right)} \right] \quad (E.12)$$

N_Fe(w) presents the concentration of iron dissolved in monoxide.

The concentration of oxygen consumed by iron in spinel oxide and monoxide could be obtained by Equation (E.13) and Equation (E.14), respectively.

$$N\_O(excess)_{spinel} = N\_Fe(v)^{*}\frac{3}{2} + N\_Fe(u)^{*}1 \quad (E.13)$$

$$N\_O(excess)_{monoxide} = N\_Fe(w)^{*}1 \quad (E.14)$$

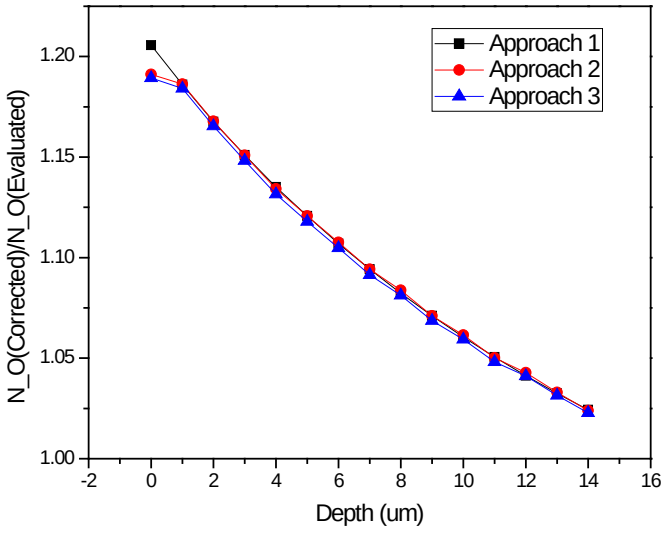

Figure E.1 Comparison of three approaches of calculation of ratio of N_O(Corrected) to N_O(Evaluated)

Appendix F. Ratio of measured oxygen concentration to evaluated oxygen concentration

There are two approaches to obtain the ratio of measured oxygen concentration to evaluated oxygen concentration for Fe-1.8Mn-1.5Cr-0.1Si alloys oxidized at 950 °C in Ar plus 5 vol.% H_2 with a dew point of 10 °C for 16 hours.

Approach 1 is to use all the measured data points to calculate the ratio of measured oxygen concentration to evaluated oxygen concentration. While approach 2 is to use only the valid measured points to calculate of measured oxygen concentration to evaluated oxygen concentration. The valid measured points are defined as those located on the oxides. Therefore, the measured points located on the base metal are not included in the calculation of N_O(Evaluated). In figure 4.15, it is obtained the average oxygen concentration in IOZ is close to 5.6 at. %. Therefore, the measured points with oxygen higher than 3 at. % are regarded as valid measured points. The average ratio of measured and evaluated oxygen is around 1.2.

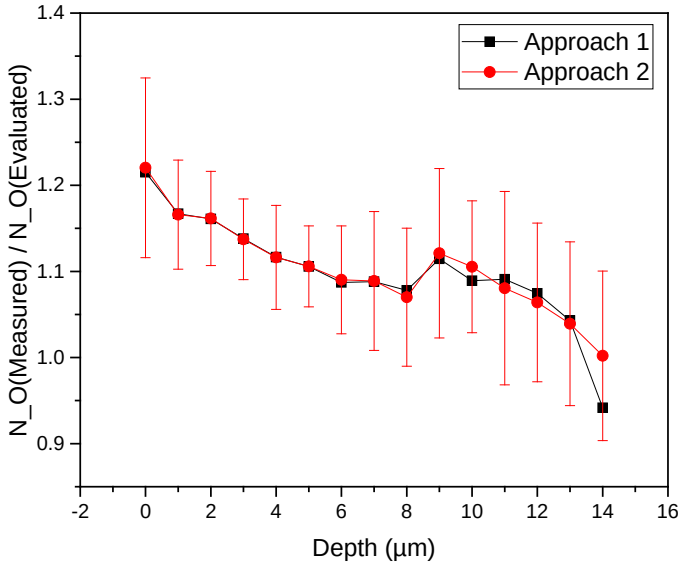

Figure F.1 The depth profiles of the ratio of measured oxygen concentration to evaluated oxygen concentration for Fe-1.8Mn-1.5Cr-0.1Si alloys oxidized at 950 °C in Ar plus 5 vol.% H_2 with a dew point of 10 °C for 16 hours.

ACKNOWLEDGEMENT

I would like to express my deepest gratitude to my supervisor Dr. ir. W.G. Sloof who was so humorous and guidance. I also want thank my daily supervisor Ir. William Mao who is always willing to help me and answer my questions. Through the process of the project, I got a lot of assistance from them with all their knowledge, time and companionship. Special thanks also to our super technical support, Kees Kwakernaak, who is very patient and precise to our research work. I would also like to convey thanks to my committee member Dr. Yaiza Gonzalez-Garcia for joining my defense. I love our group, our colleagues are always very helpful and humorous. They have kept the office always cheerful and relax.

Finally, I would like to thank my family and my dear friends who always understand and support me.